Sensitivity of Combustion Driven Structural Dynamics and Damage to Thermo-Acoustic Instability: Combustion-Acoustics-Vibration

A. Can Altunlu[1]
Mem. ASME
Section of Applied Mechanics,
Faculty of Engineering Technology,
University of Twente,
Enschede 7500 AE, Netherlands
e-mail: altunlua2@asme.org

Peter J. M. van der Hoogt
Section of Applied Mechanics,
Faculty of Engineering Technology,
University of Twente,
Enschede 7500 AE, Netherlands

André de Boer
Section of Applied Mechanics,
Faculty of Engineering Technology,
University of Twente,
Enschede 7500 AE, Netherlands

The dynamic combustion process generates high amplitude pressure oscillations due to thermo-acoustic instabilities, which are excited within the gas turbine. The combustion instabilities have a significant destructive impact on the life of the liner material due to the high cyclic vibration amplitudes at elevated temperatures. This paper presents a methodology developed for mechanical integrity analysis relevant to gas turbine combustors and the results of an investigation of the combustion-acoustics-vibration interaction by means of structural dynamics. In this investigation, the combustion dynamics was found to be very sensitive to the thermal power of the system and the air-fuel ratio of the mixture fed into the combustor. The unstable combustion caused a dominant pressure peak at a characteristic frequency, which is the first acoustic eigenfrequency of the system. Besides, the higher-harmonics of this peak were generated over a wide frequency-band. The frequencies of the higher-harmonics were observed to be close to the structural eigenfrequencies of the system. The structural integrity of both the intact and damaged test specimens mounted on the combustor was monitored by vibration-based and thermal-based techniques during the combustion operation. The flexibility method was found to be accurate to detect, localize, and identify the damage. Furthermore, a temperature increase was observed around the damage due to hot gas leakage from the combustor that can induce detrimental thermal stresses enhancing the lifetime consumption.
[DOI: 10.1115/1.4025817]

Keywords: structural dynamics, structural health monitoring, damage, combustion, thermo-acoustics, instability

1 Introduction

In modern gas turbines used for power generation, lean premixed combustion technology is generally desired to accommodate the balance between the emission targets and the efficiency. However, the gas turbine becomes more susceptible to combustion instabilities, leading to thermo-acoustic oscillations [1]. In general, particular combustion operation settings stimulate the acoustic wave propagation to form a coupling between the combustion dynamics and the structural vibrations. The variations of the pressure flow field due to the flame dynamics create pressure oscillations that can lead to thermo-acoustic instability. Basically, when the pressure and heat release are in phase, the flame acts as a strong sound source inside the combustor and amplifies the liner vibration amplitudes. When they are out of phase, the flame-sourced sound field is attenuated, leading to a stable system.

The Rayleigh criterion, which is an energy balance definition providing an explanation of the system stability, can be expressed in an integral formulation [2]

$$\int_0^\tau \int_0^V p'(x,t)q'(x,t)dtdV > \int_0^\tau \int_0^V \phi(x,t)dtdV \qquad (1)$$

where V is the volume of the domain (combustor volume), τ is the period of the oscillation, $p'$is the pressure oscillation and q' is the heat release perturbation, x is the length coordinate, t is the time, and ϕ is the wave energy dissipation. The equation is the balance criterion that states whether the net energy gained by the system (left-hand side) exceeds the sum of losses due to the radiation of the sound at the boundaries (right-hand side): instability occurs.

The loop of the thermo-acoustic feedback mechanism [1] is composed by the unsteady heat release that generates sound waves leading to acoustic oscillations and velocity fluctuations, which, in turn, perturbs the heat release (see Fig. 1). This feedback mechanism is directly linked with the structural domain of the system. The dynamic interaction within the combustor brings about the limit cycle pressure oscillations that cause elevated liner wall vibration amplitudes. The contribution of fatigue damage can become more profound in the lifetime consumption of the combustor due to the high amplitude of the cyclic wall vibrations. Damage can occur in the form of a crack initiated at possible flaws or at hot spots in the structure. The structural health must be monitored and assessed to ensure the structural integrity, durability, and reliability of the gas turbine engines for highly efficient lean combustion technologies and reduced emissions. A considerable amount of work has been published in the combustion research area in terms of fluid dynamics, improvement of efficiency, and emissions [3–8]. Furthermore, together with the published research on the thermo-acoustic instabilities in the literature [1,9–14], the coupled-domains within the thermo-acoustic feedback mechanism have been investigated to include the multiphysics such as combustion-acoustics [15,16] and acoustics-vibrations [17,18]. Recent efforts in the investigation of the interaction between combustion-acoustics-vibrations have been included in the literature [19–21], in fact their work focuses on stable combustion. Furthermore, recent efforts have been conducted in combustion

[1]Corresponding author.

Contributed by the Combustion and Fuels Committee of ASME for publication in the Journal of Engineering for Gas Turbines and Power. Manuscript received January 14, 2013; final manuscript received June 15, 2013; published online January 2, 2014. Assoc. Editor: Jerzy T. Sawicki.

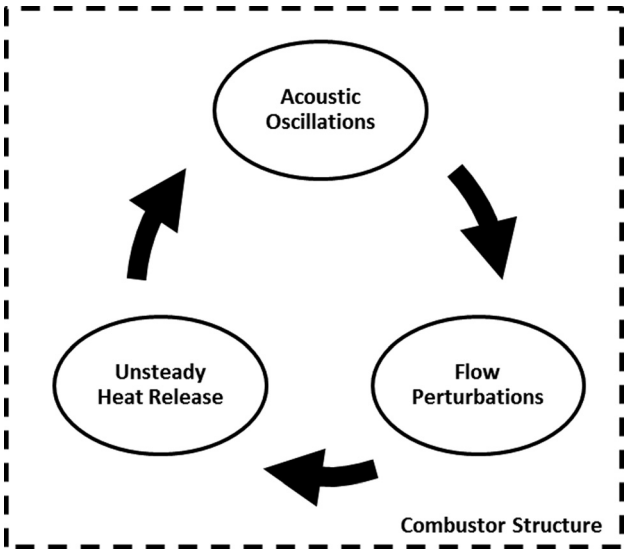

Fig. 1 The feedback mechanism of the thermo-acoustic instabilities in combustion processes

instabilities analysis to cover the two-way interaction of the fluid-structure [22–24], however, the results are not linked to structural damage conditions.

This paper presents an investigation performed in a combustor test system to explore and assess the structural dynamics characteristics, under intact and damaged conditions, altered by the dynamic two-way interaction between the oscillating pressure load in the fluid and the motion of the structure under limit cycle conditions due to thermo-acoustic instabilities. Since the complexity of the combustor system was enhanced by the existence of the multiphysical interactions and the instability phenomenon, the methodology development started with a sample problem with well-defined initial and boundary conditions. Section 2 presents the results of the experimental, analytical, and coupled/uncoupled numerical approaches used for modal characterization of the sample problem. Furthermore, the validation of the structural health monitoring techniques is described and the findings are stated in the Sec. 2.8. In Sec. 3, the design of a laboratory-scaled generic combustor and the adopted methods and materials are presented. In addition, the application of the methods to the combustor test setup is described with an emphasis on linking the structural dynamics, acoustics, and combustion dynamics. Then, the results on the analysis of the combustion-driven structural life consuming phenomena due to the combustion instability are presented. In the final section, the results are summarized and the conclusions are drawn.

2 Sample Problem: Aero-Box

In this section, the structural and acoustic characterization of a simplified test setup, the so-called aero-box, using analytical, numerical, and experimental approaches is presented. Subsequently, the applied structural health monitoring techniques are described. The aero-box is a fairly stiff structure with well-defined test and boundary conditions [25]. Therefore, tests under both intact and damaged conditions provide a basic understanding of the relation between the eigenfrequencies, mode shapes, flexibility, and damage state. Lastly, this section is concluded by discussing the structural response and damage state in the aero-box as along with the challenges of applying the methods to the combustor test setup.

2.1 Design of the Aero-Box. The structural responses of intact and damaged flexible plates are explored in the aero-box shown in Fig. 2. The dimensions, front view, side view, and the damaged flexible plate, including an initial center-crack with length a_o in the total assembly, are illustrated in Figs. 2(*a*)–2(*d*), respectively.The test system consists of a hollow aluminum box with 30 mm thick walls, a 30 mm thick plate to cover the top of the box, and an excitation source, a loudspeaker. The loudspeaker inside the box generates an interior sound field resulting in the vibration of the flexible plate that can be attached to the front side of the box. The aero-box has a high stiffness to avoid any interaction between the plate and the aero-box, whose first eigenfrequency is 1270 Hz. The aluminum plate material properties are: a Young's modulus (E) of 70.5 GPa, Poisson's ratio (υ) of 0.3, and density (ρ) of 2700 kg/m^3. The flexible plate was attached to the box by reinforcement strips bolted to the box; thus satisfying a 'clamped on all edges' condition. The dimensions of the plate are: 160 mm in width, 210 mm in height, and 1.1 mm in thickness. A slot-type crack was machined in the plate until the cutting tool-tip reaches the next surface across the thickness. Note that the crack in the damaged plate configuration is not a through-thickness-crack but a deep-surface-crack with a 35 mm initial crack length and a 3 mm crack width.

2.2 Analytical Model. Analytical equations were used to obtain the structural and acoustic eigenfrequencies in order to validate the experimental and numerical results. The eigenfrequencies of the first six modes of the rectangular plate were analytically calculated by [26]

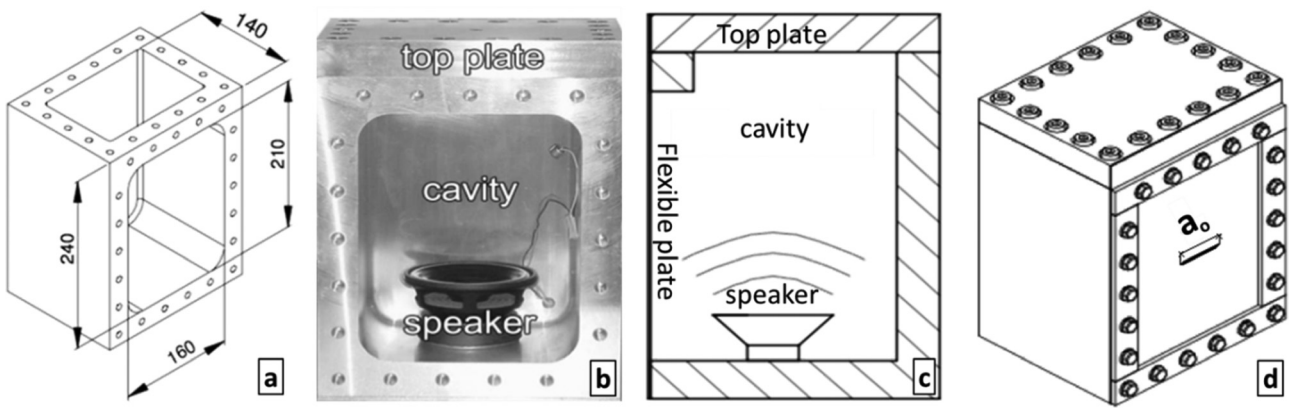

Fig. 2 The dimensions and the configuration of the aero-box

Table 1 The interpolated values for λ_{ij}^2

	Mode sequence					
	1	2	3	4	5	6
λ_{ij}^2	29.58	50.8	68.22	78.49	94.64	109.84
(ij)	$S(1,1)$	$S(2,1)$	$S(1,2)$	$S(3,1)$	$S(2,2)$	$S(3,2)$

$$f_{ij} = \frac{\lambda_{ij}^2}{2\pi L_p^2}\sqrt{\frac{EB_p^3}{12\gamma(1-v^2)}} \tag{2}$$

where λ_{ij} is the dimensionless frequency parameter of the rectangular plates, which is a function of the boundary conditions applied to the plate and the aspect ratio of the plate (defined as the length to width ratio), L_p is the length and B_p is the thickness of the plate, and γ is the mass per unit area of the plate ($\gamma = \mu^* B_p$ with density ρ). The aspect ratio of the flexible plate is 0.762 and the λ_{ij}^2 values were interpolated between aspect ratios of 2/3 and 1.0. The λ_{ij}^2 values for a clamped on all edges condition are listed in Table 1 [26]. The calculations were performed under the assumption that the influence of the air to the dynamic behavior of the flexible plate is negligible.

The acoustic eigenfrequencies of the aero-box can be analytically calculated considering a closed rectangular volume (acoustic cavity) with acoustically hard walls by the following equation [26]:

$$f_{ijk} = \frac{c}{2}\sqrt{\left(\frac{i}{L_x}\right)^2 + \left(\frac{j}{L_y}\right)^2 + \left(\frac{k}{L_z}\right)^2} \tag{3}$$

where c is the speed of sound, i, j, and k are the number of half waves in the three length directions (L_x, L_y, L_z) associated with the x, y, and z coordinates (160, 240, and 140 mm), respectively. The analytical calculation results for both the structural $S(i,j)$ and acoustic $A(i,j,k)$ modes are listed in Table 2.

2.3 Acousto-Elastic Interaction. The interaction between the fluid and structure can be apparent since the dynamic behavior of the structure is evidently influenced by the media in contact. The eigenfrequencies and mode shapes can be altered due to the coupled mechanism. Thus, the coupling between the acoustic volume and the adjacent structure domain was analyzed by the finite element method (FEM). The acousto-elastic interaction analysis includes acoustic elements to represent the acoustic pressure waves in the cavity and shell elements to enable the displaced motions of the structure. The acoustic and the structure mesh are coupled at the interface, which ensures the exchange of the fluid and structural loads between the acoustic and structure domains. Thus, the acoustic pressure-driven structural displacements and, hence, the bounce-back generation of an effective fluid load due to these motions are provided. The general governing equations of the system [27] can be written in the following form:

$$\mathbf{M}^f\ddot{\mathbf{P}} + \mathbf{K}^f\mathbf{P} = \mathbf{F}_f - \rho_o\mathbf{C}^T\ddot{\mathbf{u}} \tag{4}$$

$$\mathbf{M}^s\ddot{\mathbf{u}} + \mathbf{K}^s\mathbf{u} = \mathbf{F}_s - \mathbf{C}\mathbf{P} \tag{5}$$

where $\mathbf{P}$ is the nodal pressure vector, $\mathbf{u}$ is the nodal displacement vector, $\mathbf{M}^f$ is the assembled fluid equivalent "mass" matrix, $\mathbf{K}^f$ is the assembled fluid equivalent "stiffness" matrix, $\mathbf{M}^s$ is the assembled structural mass matrix, $\mathbf{K}^s$ is the assembled structural stiffness matrix, ρ_o is the density, and $\mathbf{C}$ is the so-called coupling matrix, which represents the effective surface area composed by the nodes at the interface. In the interface surface, the vector containing the nodal displacements is associated with the fluid domain and the vector containing nodal pressures is associated with the structural domain through the coupling matrix. Thus, the exchange of the quantities is included within each domain. The coupled acoustic and structural problem takes the following form [28]:

$$\begin{bmatrix}\mathbf{M}^s & \mathbf{0}\\ \mathbf{M}^{fs} & \mathbf{M}^f\end{bmatrix}\begin{Bmatrix}\ddot{\mathbf{u}}\\ \ddot{\mathbf{P}}\end{Bmatrix} + \begin{bmatrix}\mathbf{K}^s & \mathbf{K}^{fs}\\ \mathbf{0} & \mathbf{K}^f\end{bmatrix}\begin{Bmatrix}\mathbf{u}\\ \mathbf{P}\end{Bmatrix} = \begin{Bmatrix}\mathbf{F}^s\\ \mathbf{F}^f\end{Bmatrix} \tag{6}$$

where $\mathbf{M}^{fs} = \rho_o\mathbf{C}^T$ is the assembled fluid-structure coupling "mass" matrix, $\mathbf{K}^{fs} = -\mathbf{C}$ is the assembled coupling "stiffness" matrix, $\mathbf{F}^s$ and $\mathbf{F}^f$ are the structural and fluid load vectors, respectively. In the finite element representation, the shared nodes at the interface are equipped by the displacement and pressure degrees of freedom and the acoustic domain assumes that the fluid is compressible and inviscid and no mean flow velocity is considered. The mean fluid density and the pressure are uniform in the acoustic field. The calculated eigenfrequencies from the coupled and uncoupled FEM can be seen in Table 2.

Table 2 Test setup eigenfrequencies (Hz) with the intact plate

Mode number	Measured	Analytic	FEM uncoupled	FEM coupled
$S(1,1)$	309	310 (0.3%)	306 (1.0%)	311 (0.6%)
$S(2,1)$	515	532 (3.3%)	519 (0.8%)	514 (0.2%)
$S(1,2)$	704	714 (1.4%)	715 (1.6%)	710 (0.9%)
$A(1,0,0)$	744	715 (3.9%)	734 (1.3%)	732 (1.6%)
$S(3,1)$	858	822 (4.2%)	868 (1.2%)	864 (0.7%)
$S(2,2)$	901	991 (10.0%)	911 (1.1%)	905 (0.4%)
$A(0,0,1)$	1087	1072 (1.4%)	1107 (1.8%)	1103 (1.5%)
$A(0,1,0)$	1232	1225 (0.6%)	1253 (1.7%)	1254 (1.8%)
$S(3,2)$	1235	1150 (6.9%)	1241 (0.5%)	1236 (0.1%)
$S(1,3)$	1310	—	1338 (2.1%)	1338 (2.1%)
$A(1,0,1)$	1333	1288 (3.4%)	1362 (2.2%)	1347 (1.1%)

2.4 Modal Characterization. Experiments were performed on the aluminum flexible intact plate to examine the dynamic modal parameters (eigenfrequencies and mode shapes). The surface vibrations of the plate were scanned by a laser Doppler vibrometer (LDV) at 9×9 measurement grid points on the plate, which was found to be the optimum scan grid for an accurate analysis. Hereafter, this technique will be called the vibration-based (VB) technique.

The experimental, analytical, and numerical results for the structural eigenfrequencies are listed in Table 2. The (percent) deviation in the results compared to the measured results is written in parentheses. Note that the value in parentheses in the presented tables represents the deviation of the corresponding result throughout this paper. The calculated eigenfrequencies show some deviation from the measurements; nonetheless, the coupled FEM provides better predictions in general. The deviation in the structural eigenfrequencies of the plate for the analytical calculation can be caused by the interpolation of the λ_{ij} values obtained from the literature. Note that $S(1,3)$ is not included in the list, since this mode is out of the given λ_{ij} range. Besides, the interior of the aero-box was machined from a single piece aluminum slab that contains fillets on the corners. In addition, the loudspeaker placed inside the aero-box occupies a space and reduces the acoustic volume and influences the acoustical behavior in the cavity [25]. The differences in the acoustic eigenfrequency results can be attributed to the fact that the interior volume is slightly different from the theoretical rectangular box volume in the analytical calculations. In the numerical models, the bolt connection of the plate and the frame, which was modeled as bonded-connection (perfectly clamped), and the presence of the loudspeaker, which was not modeled, can cause a deviation.

The experimental and numerical results for the mode shapes are depicted in Fig. 3 for the intact plate configuration. The

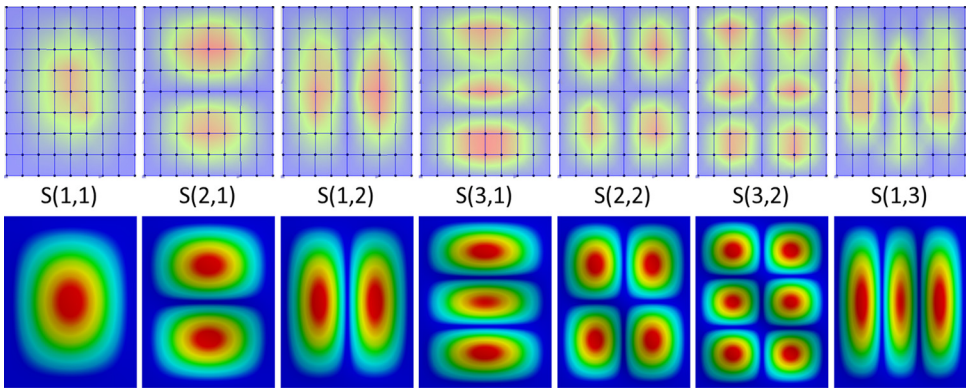

Fig. 3 Experimental (above) and numerical (below) results for the mode shapes of the intact plate configuration

experimentally predicted mode shapes show an excellent match with the numerical calculations.

2.5 Structural Damage Detection. Structural response monitoring and damage/fault detection at the earliest possible stage is crucial to assure the safety of the component, assess the residual lifetime, plan the required maintenance intervals, and set the inspection requirements. Vibration-based damage monitoring is one of the nondestructive methods used to examine the dynamic properties of the structures. Basically, the vibration-based method tracks the alterations of the modal parameters due to possible damage such as eigenfrequencies, mode shapes, modal damping, modal strain energy, and flexibility [29–40]. Much research has been conducted on the frequency shifts for damage prognostics [31,39]. The statistical variation of the eigenfrequencies is less than the other modal parameters in the case of random error sources [41,42]; nevertheless, the feasibility of this technique can be enhanced by picking up the most sensitive eigenfrequencies to damage. Those selected eigenfrequencies reduce the necessary monitoring locations and indicate damage while other modes can remain insensitive. However, the frequency shift monitoring can be misleading in some cases when damage in the structure reshapes and rearranges the mode shapes in such a way that the eigenfrequency of interest actually loses its sequence within the mode numbers and swaps with the new eigenfrequency [43]. Therefore, the mode shape information, together with the eigenfrequencies, can provide better accuracy in health monitoring. The location of the damage in the geometry can be determined by pursuing the changes in the measured flexibility of the structure. The localization is based on the comparison of the flexibility matrixes using the mass-normalized mode shapes and eigenfrequencies of the intact and the damaged structure. The flexibility matrix [37,38] is inversely proportional to the square of the eigenfrequencies; therefore, the flexibility matrix is very sensitive to the changes in the low frequency modes of the structure.

2.6 Damage Detection by Frequency Shift Method. A center-crack, as described in Sec. 2.1, was introduced in the plate. The eigenfrequencies of the damaged plate were measured using the VB technique. The results were cross checked by the so-called acoustic emission (AE) technique, which is elastic radiation generated by the rapid release of energy from sources within the material (plate) under an external excitation source (loudspeaker). Therefore, a microphone was used instead of the LDV for the measurement. The alteration of the first seven eigenfrequencies due to the damage state in the plate is presented in Table 3. The VB and AE monitoring techniques applied to the damaged plate show a very good match. The structural stiffness decreases due to the damage; as a result, the eigenfrequencies decrease in the damaged case, as seen in the table.

Table 3 Eigenfrequencies (Hz) of the intact and damaged plate

Mode number	Intact plate (VB)	Damaged plate (VB)	Damaged plate (AE)
$S(1,1)$	309	299 (3.2%)	300 (2.9%)
$S(2,1)$	515	509 (1.2%)	510 (1.0%)
$S(1,2)$	704	693 (1.6%)	694 (1.4%)
$S(3,1)$	858	838 (2.3%)	837 (2.4%)
$S(2,2)$	901	900 (0.1%)	898 (0.3%)
$S(3,2)$	1235	1227 (0.6%)	1225 (0.8%)
$S(1,3)$	1310	1282 (2.1%)	1283 (2.1%)

A sensitivity analysis was performed to obtain the most sensitive mode to the current damage configuration by calculating the difference in the structural eigenfrequencies between the intact and damaged plate. The results for the VB and AE techniques are shown in Fig. 4. Mode 1, $S(1,1)$, was found to give the most distinguishable response to the damage because the introduced damage (center-crack) is positioned on one of the node points within the mode shape.

A numerical analysis was carried out to predict the mode shapes of the damaged plate configuration, which is described in Sec. 2.1. The comparison of the mode shapes between the intact and damaged cases is presented in Fig. 5. As seen from the figure, the presence of the center-crack causes a swap between modes $S(1,3)$ and $S(4,1)$ and deterioration in the mode shapes of some higher modes, in which the crack location coincides with the node points of the particular mode. The actual deviation in mode $S(1,3)$

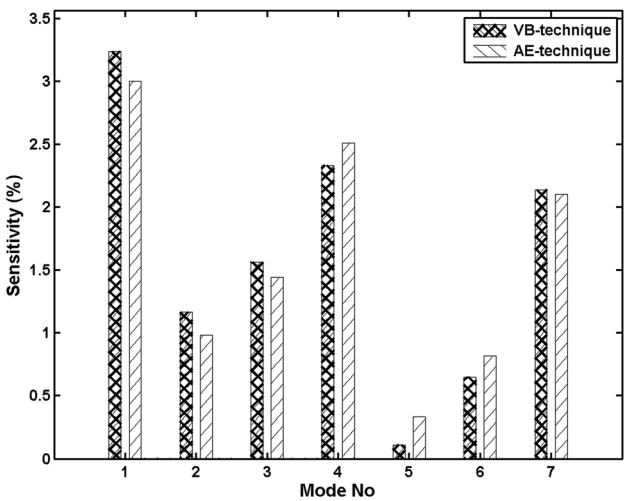

Fig. 4 Sensitivity analysis on the eigenfrequencies

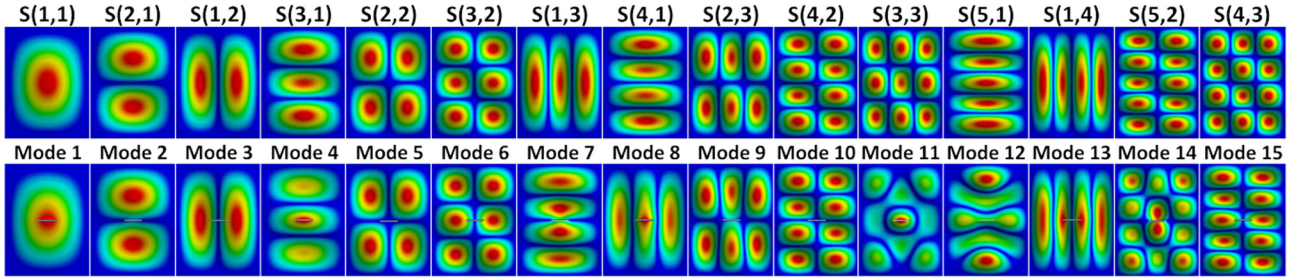

Fig. 5 Damage sensitivity of mode shapes (top: intact and bottom: damaged)

with respect to the damage is hindered, since the two adjacent modes exchange their modal sequence. In conclusion, the most sensitive mode is very much dependent on the damage location and the orientation; therefore, the selection of the mode to monitor is crucial to be able to capture the small changes in the dynamic structural properties. However, damage detection by the frequency shift method can be misleading since the mode sequence can reshuffle due to the damage configuration.

2.7 Damage Localization by Flexibility Method. The system stiffness matrix is more sensitive to higher modes than lower modes; thus obtaining the accurate dynamic stiffness matrix requires measuring a significant amount of higher modes [44]. However, experimentally extracting higher modes of the system is challenging due to practical limitations. On the contrary, the flexibility matrix, which is defined as the inverse of the stiffness matrix, is inversely related to the square of the natural frequencies; hence, higher modes contribute less to the flexibility matrix. Instead, it is more sensitive to the changes in lower modes. The flexibility method is based on the change of the flexibility matrix, which is composed of the mode shape and the reciprocal of the natural frequency. In theory, the structural damage reduces the stiffness [45] and increases the flexibility. The responsiveness of the flexibility matrix to a structural deterioration serves as a good indicator in structural health monitoring. The homogeneous dynamic equilibrium equation can be expressed as

$$\mathbf{K}\boldsymbol{\Phi} = \mathbf{M}\boldsymbol{\Phi}\boldsymbol{\Omega} \tag{7}$$

where $\mathbf{K}$ is the stiffness matrix, $\mathbf{M}$ is the mass matrix, $\boldsymbol{\Phi} = [\Phi_1, \Phi_2, \ldots, \Phi_n]$ is the mode shape matrix where the mode-shape vectors are mass-normalized to unity as $\boldsymbol{\Phi}^T\mathbf{M}\boldsymbol{\Phi} = \mathbf{I}$, $\boldsymbol{\Omega} = \text{diag}(\omega_i^2)$ is the modal stiffness matrix, $i\ (=1,\ldots,n)$ is the mode shape number indicator, n is the number of degrees of freedom, and ω is the modal frequency. The flexibility matrix, $\mathbf{G}$. related to the modal data can be derived as [44]

$$\boldsymbol{\Phi}^T\mathbf{K}\boldsymbol{\Phi} = \boldsymbol{\Phi}^T\mathbf{M}\boldsymbol{\Phi}\boldsymbol{\Omega} \tag{8}$$

$$\mathbf{G} = \mathbf{K}^{-1} = \boldsymbol{\Phi}\boldsymbol{\Omega}^{-1}\boldsymbol{\Phi}^T = \sum_{i=1}^{n} \frac{1}{\omega_i^2}\boldsymbol{\Phi}_i\boldsymbol{\Phi}_i^T \tag{9}$$

The change in the flexibility matrix with respect to the initial reference data set for the intact case and the data set for the damaged case is given by

$$\mathbf{G}_\Delta = \delta_{im} = \mathbf{G}_h - \mathbf{G}_d \tag{10}$$

where $\mathbf{G}_\Delta$ is the change in the flexibility matrix and $\boldsymbol{\delta}_{im}$ are the elements of $\mathbf{G}_\Delta$. Here, $\mathbf{G}_h$ and $\mathbf{G}_d$ are the intact and damaged case flexibility matrices, respectively. The parameter used to detect and locate the damage in the structure is the degree of change in the flexibility for each measurement location. It can be characterized by [37]

$$\bar{\delta}_m = \max_i |\delta_{im}| \tag{11}$$

where $\bar{\delta}_m$ is the maximum absolute value of the elements in each corresponding column in $\mathbf{G}_\Delta$ and m is the degree of freedom. The presence of the damage reduces the stiffness of the structure and the flexibility is the inverse of the stiffness. Thus, the structural response of the plate alters as damage occurs by increasing the local flexibility of the structure. The damage in the flexible aluminum plate was detected and localized by comparing the flexibility matrices of the intact and damaged cases shown in Fig. 6. Since the slot-type crack machined into the specimen is not through-thickness, yet a deep-surface-crack, in the figure the change in the local flexibility is concentrated at the damage location and the traces to the sides are visible representing the transversely.aligned center-crack configuration.

2.8 Discussion on the Aero-Box. The applicability of the methodology was verified and validated in a sample problem: the so-called aero-box. Two cases, for intact and damaged plates, were investigated to assess the structural health monitoring methods. Both the VB and AE techniques provide a noncontact structural health monitoring, however, the VB technique is superior in overcoming the challenges of elevated temperature conditions, high amplitude loading, and harsh environment conditions due to the combustion process. The damage was detected using the frequency shift method and the most sensitive eigenfrequency to the damage configuration was found. Moreover, the location and the severity of the damage were also predicted using the flexibility method. The results of this method show that identification of the modal parameters enables the construction of the flexibility matrix. The change in the measured entities of the matrices between the initial reference intact case and damaged case was captured to detect and localize the damage. Both damage monitoring methods can be performed using only the test data, without requiring any additional models for the structure. However, the field-of-interest in the structure should be determined with hot spot analysis to

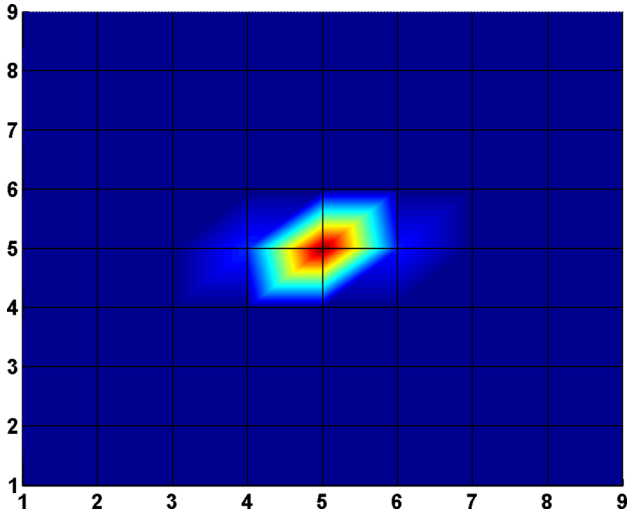

Fig. 6 Damage localization by the flexibility method

avoid a full modal analysis. Thus, the flexibility method can be used for damage localizations accompanying the frequency shift method, which can be applied on a single measurement point, excluding the node points of the most sensitive mode, to detect the presence of the damage. It should be highlighted that with regard to the measurements, the acousto-elastic fully coupled finite element model was found to be more accurate, in general, compared to the analytical and uncoupled FEM calculations. This result indicates the existence of an interaction between the enclosed acoustic volume and the flexible structure that is also observed in combustors [46]. The outcome of this study was utilized as a reference to describe the behavior of the complex combustor system, for which the investigation is presented in the next section.

3 Laboratory-Scaled Generic Combustor Test Setup

In this section, the investigation of the impact of the combustion driven limit cycle oscillations on the structural properties under the intact and damaged conditions is presented. The methodology described in the previous section is utilized for a laboratory-scaled generic combustion test system. For this purpose, a test combustor setup [47] depicted in Fig. 7, which can be modified to generate stable and unstable combustion conditions, was utilized in this research. Two geometric configurations of the combustor were investigated; namely, a single liner combustor and a double liner combustor. In the latter configuration, the limit cycle oscillations were observed due to the combustion instabilities. In this configuration, the acoustic field was enlarged by doubling the liner length and, consequently, the acoustic eigenfrequencies of the combustor decreased inversely proportional to the length. The first acoustic eigenfrequency was excited by the combustion process and the resulting pressure oscillations were generated. The materials used in the combustor and their compliance are described in the next sections with an emphasis on the similarities to a typical combustor base material. Next, a comparative investigation on the combustion stability, considering the operational input parameters and the liner length, is presented. Finally, the results are linked to the structural dynamics of the intact and damaged cases.

Table 4 Combustor test system dimensions

Section	Dimension (mm)
Combustor outer width	158
Upstream outer depth	33
Downstream outer depth	58
Wall thickness	4
Quartz glass thickness	5
Specimen thickness	1

3.1 Design of the Combustor. In Fig. 7, the single ($S3$) and double liner ($S3 + S4$) configurations of the test combustor are depicted and the dimensions are listed in Table 4. The marks indicated as 'p' designate the gas pressure and temperature and the liner surface vibration measurement locations. The combustor was designed as a Rijke tube configuration consisting of mainly two sections: the acoustically closed upstream and the downstream (flame-box and the liner). The upstream section ($S1$) consists of an air-feeding box, a rectangular duct with a 25×150 mm hollow cross-sectional area and 275 mm long, and an equilateral triangular wedge as a flame holder, where methane, as the fuel, is injected through the holes on both sides (see Fig. 8). The downstream section consists of a flame-box ($S2$) and a rectangular liner ($S3$ and $S4$). The flame-box is surrounded by four quartz glass windows providing an optical access to the flame. The rectangular geometry eases assembly of the glass windows. Additionally, the glass windows can be replaced by an intact or a damaged test specimen to investigate the structural dynamics during the operation while visualizing the flame through the side windows. The turbulent flame is technically premixed and flame stabilization takes place on the wedge wake in the combustor test system. The combustor is supported from the bottom of the flame-box.

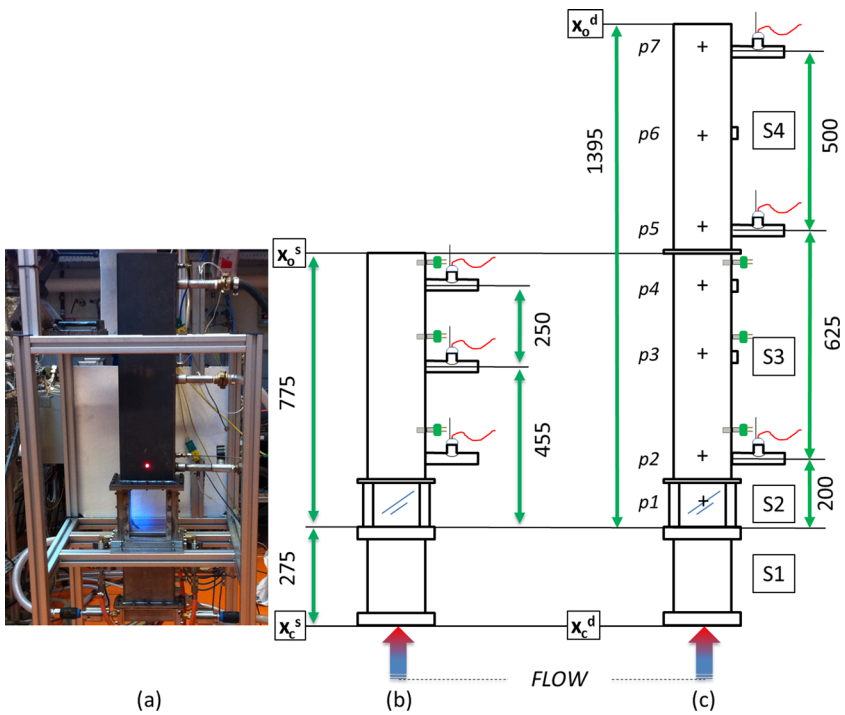

Fig. 7 Combustor test system: (*a*) and (*b*) single, and (*c*) double liner configurations (upstream section (*S*1), flame-box (*S*2), and a rectangular liner (*S*3 and *S*4))

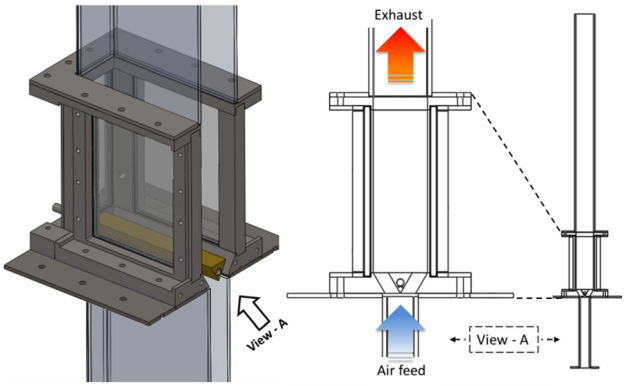

Fig. 8 Combustor flame-box and wedge

3.2 Material Compliance and Properties. During the combustion process, the liner is exposed to elevated temperatures; therefore, the influence of the temperature levels on the structural properties becomes crucial. The combustor liner and the flame-box are made of austenitic stainless steel (AISI) Type310. Type316 was chosen as the specimen material that has sufficiently enough heat and corrosion resistance at the test temperatures within a relatively short exposure time and well established properties. Since the specimen was replaced with a new one in every new experiment, this material serves satisfactorily for the test purposes with its cost-effectiveness. The compliance of the test material can be seen in Fig. 9 in comparison to a typical combustor base material: the nickel-base superalloy Alloy230 (Haynes230) [48,49]. The materials used in the test setup exhibit analogical trends to the Alloy230 and satisfactory properties within the experimental conditions. In the three materials, the effect of the temperature on the thermal expansion and elastic modulus is fairly proportional, whereas the ultimate tensile strength dramatically decreases beyond 900 K. There is a clear switch due to the transition from normal low temperature mechanisms to creep controlled mechanisms, as can be observed from the drastic decline in the stress to rupture time curve.

3.3 Specimen Configuration. The dimensions of the test specimen used in the combustor are $150 \times 108 \times 1$ mm, in length (L), width (W), and thickness (B), respectively. The damage on the specimen is represented by a center-hole 6 mm in diameter (d_c) and an adjacent crack was machined towards its length direction of 6 mm to each side that creates a crack length of 18 mm (a_c) and the crack width is 1 mm (w_c). The geometric representation of the specimen, the introduced damage, and the assembly of the flame-box can be seen in Fig. 10. The numbered items in the figure, respectively, are: gaskets (1), the supporting frame (2), quartz glass or specimen (3), liner (4), flame-box (5), upstream (6), and damage configuration (detail-Z). The hatch area shown in the specimen geometry (3) is the contact area with the gaskets and, hence, sandwiched by the supporting frame and the flame-box.

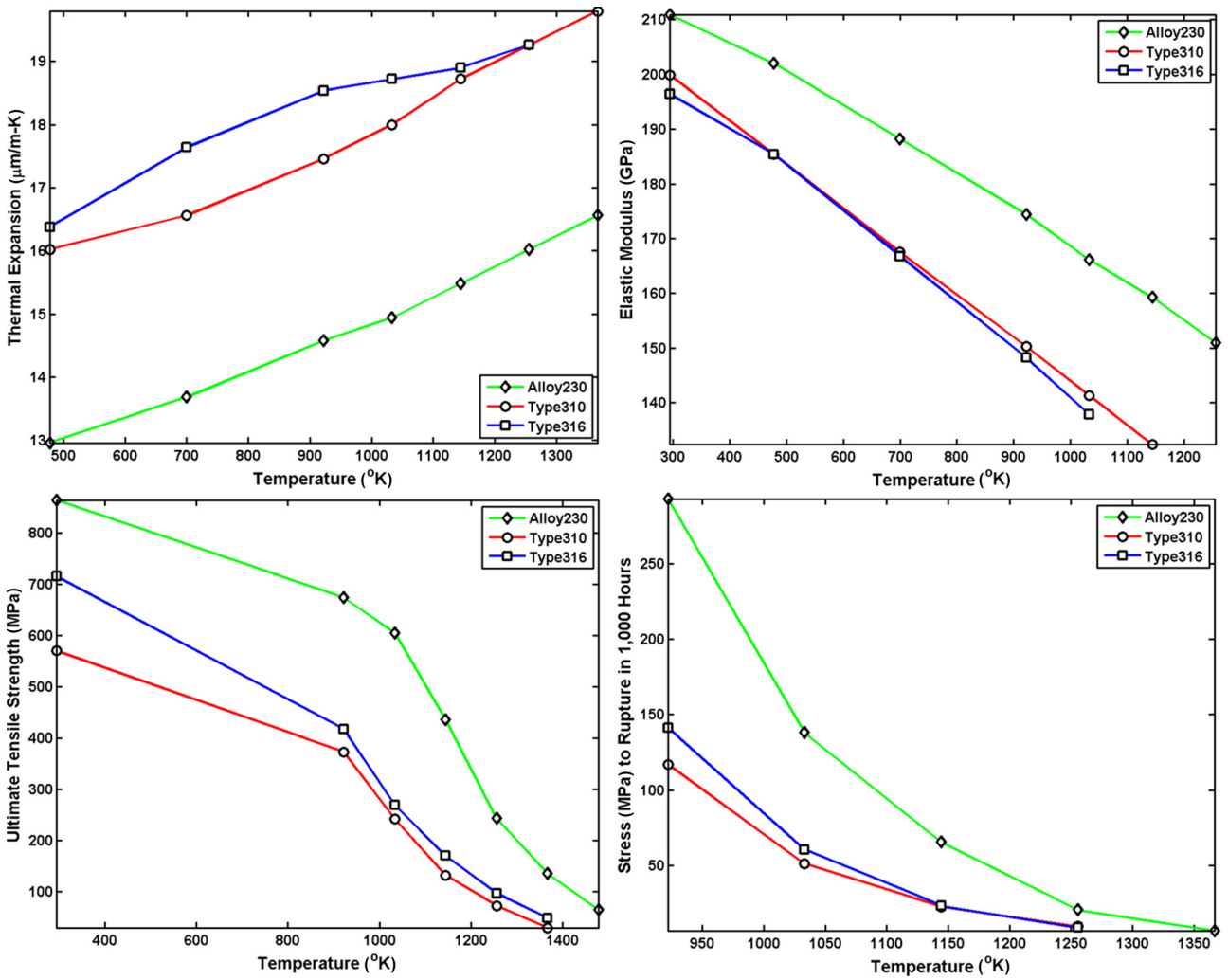

Fig. 9 Temperature dependence of the material properties

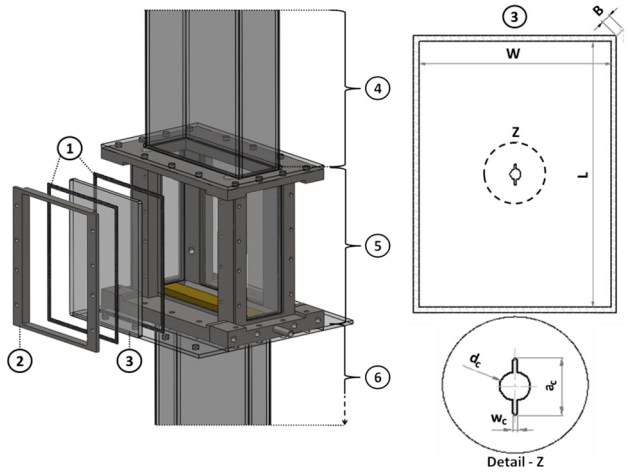

Fig. 10 Flame-box assembly and specimen configuration

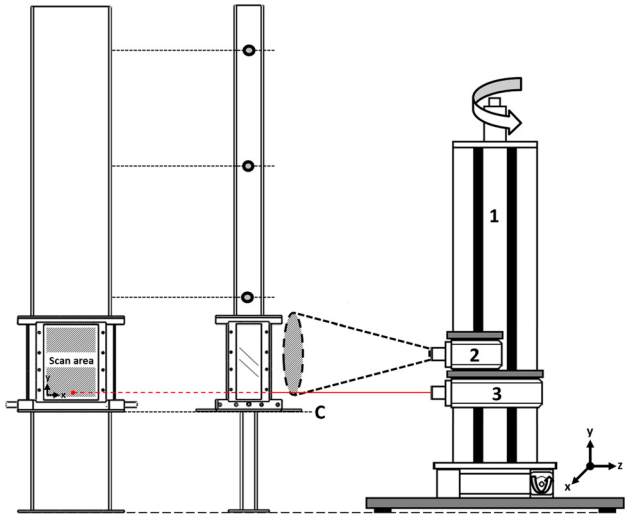

Fig. 12 Schematic representation of the structural condition monitoring system

3.4. Instrumentation. The structural modal characterization tests were performed on the combustor test setup as a bare structure to link the structural dynamics later in the combustion experiments (see Fig. 11). The two experimentation procedures will be mentioned as the cold and hot cases, respectively.

In the cold case, the vibration modes of the combustor test system were analyzed by two methods: the roving hammer impact test and the shaker test. In the roving hammer test, an accelerometer was placed at a single degree of freedom (DOF) and an impact hammer was used to excite at the measurement grid (DOFs). The shaker test includes the electromechanical shaker to excite the system at a fixed reference point and the LDV was used to travel between the measurement grid points. The shaker was attached to the combustor liner with a stinger that enables the applied force to be aligned along the stinger axis. The generated random noise excitation was characterized by a force transducer. The frequency response functions between the measured wall velocity and the excitation force were recorded by a data acquisition and an analyzer system (Siglab). A software package (ME'scopeVES) was used to extract the modal parameters.

The combustion tests for the hot case covers the combustor inner temperature, pressure, and liner wall velocity recordings and the combustor surface temperature measurement by an infrared (IR) camera. The temperature inside the combustor was measured by K-type thermocouples. The dynamic pressure measurement sensors were attached in the side-tubes that are connected to the semi-infinite hoses and external coolers were directed towards the devices. This technique overcomes the high temperature effects to the piezoelectric pressure transducers and provides nonreflecting acoustic conditions. The liner wall vibration was recorded by a LDV via a data acquisition system, DAQ (National Instruments). The mass flow controllers for fuel and for air were used and the flow was controlled by a PC via the LabVIEW program [50]. The vibration analysis of the specimen attached to the flame-box (Fig. 10) was utilized by the LDV mounted on a traverse system that enables automated measurements (Fig. 12).

3.5 Structural Condition Monitoring. The structural health monitoring system is depicted in Fig. 12, including the LDV (3) for vibration characterization and the IR camera (2) for thermal characterization mounted on a programmable traverse system (1), which can slide in the *x-y* plane. In the figure, the clamping position of the test setup is denoted as "C." Since the combustor environment is harsh at a high temperature and elevated vibration levels exist due to the unstable combustion process, a noncontact vibration-based damage monitoring method was utilized to analyze the structural dynamics and the health of the combustion liner during operation (Fig. 11). The technique used here is capable of detecting the presence of damage, localizing and quantifying the severity of the damage by examining changes in the measured dynamic response of the structure.

3.6 Combustion-Driven Dynamics. Four test cases were carried out in the test system, as listed in Table 5. In the investigation, two test system configurations (single and double liners) are included, as described in Sec. 3.1, and the initial operation setting varies from 40 to 60 kW for the thermal power and from 1.4 to 1.6 for the air-fuel (equivalence) ratio, which is the mass ratio in the mixture normalized by the stoichiometric air-fuel ratio.

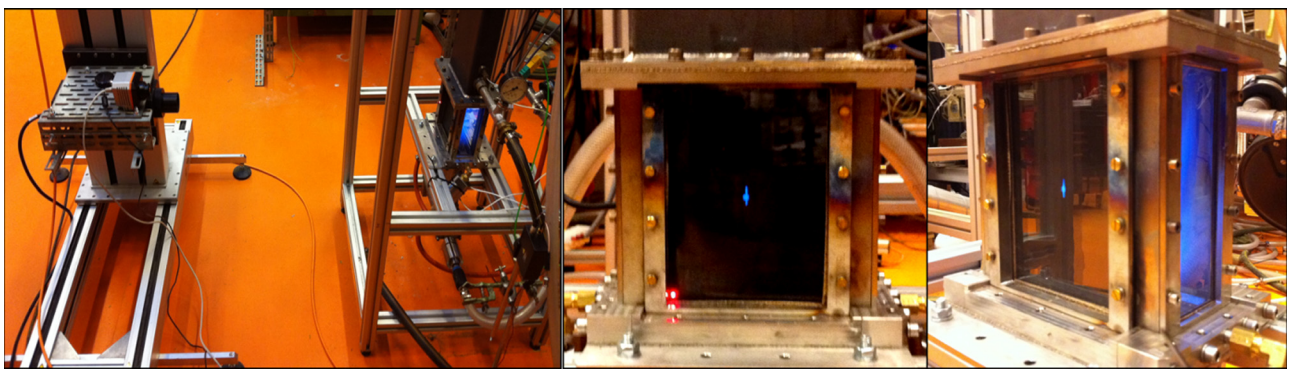

Fig. 11 Laser surface scan on the damaged specimen mounted in the flame-box

Table 5 Combustion test cases

Case code	Thermal power (kW)	Air-fuel ratio	Test system configuration	Combustion stability
Case 11	40	1.4	Single liner	Stable
Case 12	60	1.6	Single liner	Stable
Case 21	40	1.4	Double liner	Stable
Case 22	60	1.6	Double liner	Unstable

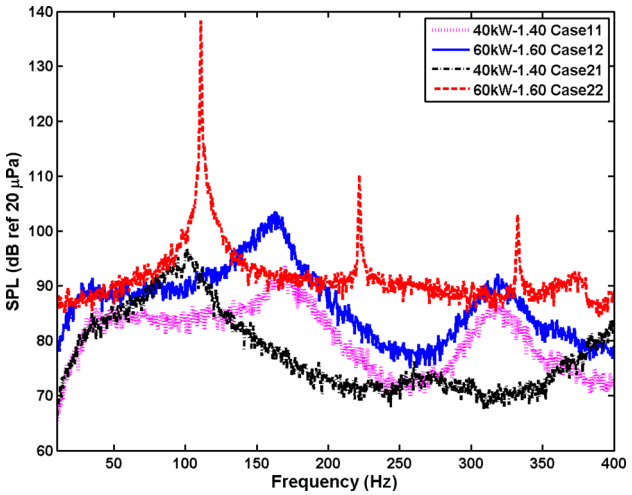

Fig. 13 Pressure spectrum of the combustor

In Fig. 13, the pressure spectrum for the test cases is shown. There was no limit cycle regime observed in the case 11, case 12, and case 21, in which the flame was stable and generated a low-level combustion noise only. Instability was observed, however, in case 22 at the frequency of 111 Hz while the pressure amplitude inside the combustor was around 160 dB. The frequency of the acoustic pressure at the flame excites the first acoustic mode of the combustor that induces the instability. The acoustic characterization is presented in the next section (see Tables 6 and 7). Furthermore, the system generates characteristic frequencies as the higher-harmonics of the limit cycle frequency at 222 Hz and 333 Hz. These visible peaks are considered as the higher-order modes of the system [14,51]. Note that the pressure signals are obtained from the transducer located at the top measurement location for all cases. Recalling the combustor test system design (see Fig. 7), the three pressure transducers were mounted at the bottom, middle, and top locations of the liner length. In the single liner configuration, these measurement points correspond to $p2$, $p3$, and $p4$, whereas the $p2$, $p5$, and $p7$ locations are used in the double liner configuration.

A stability map containing nine operating points was created in terms of the thermal power and air-fuel ratio to characterize the combustor (see Fig. 14). In the figure, the combustion process tends to become unstable with an increasing air-fuel ratio for a leaner mixture combustion and with increasing power. A transition line is observed that divides the map into stable and unstable operating zones. The operating points on the transition line

Table 7 Characteristic acoustic frequency (Hz) of the single and double liner configurations

Test temperature	Experimental	Analytical	FEM	Analytical†	FEM†
${}^{(s)}T_{60\text{-}1.6}$	163	165 (1.2)	175 (7.4)	161 (1.2)	170 (4.3)
${}^{(d)}T_{60\text{-}1.6}$	111	104 (6.3)	112 (0.9)	102 (8.1)	110 (0.9)
Difference (%)	32	37	36	37	35

Note: the superscript symbol '†' denotes the end correction.

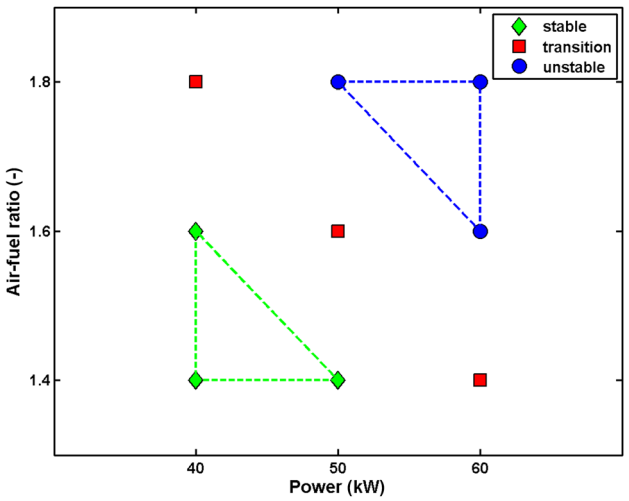

Fig. 14 Stability map for the double liner configuration

implied a dynamic system characteristic, including two different combustion regimes: stable and unstable. A bifurcation at these certain operating conditions can occur depending on the initial operation setting, air-fuel ratio, and power as in this work, due to the sequential direction of the test points (initial operation settings) that indicates the nonlinear characteristics of combustion instabilities [52].

The surface temperatures were measured at the same locations ($p1$, $p2$, $p3$, and $p4$) for the cases 22 and 12 that have the same initial operation settings (see Fig. 7). The liner surface temperature profile and the flame profiles are depicted in Fig. 15. The maximum surface temperature is measured as 370 °C for case 22 and 245 °C for case 12. Since the test system is technically uncooled, the main heat transfer processes are the radiation heat flux from the gas, the convection heat flux from the gas, the conduction heat flux across the wall thickness, and the convection heat flux to the surrounding air. In the figure, taking into account the energy balance, the trend of the curves can be considered as a comparative indicator for the flame height that exhibits a bend-down at the '$p3$' location in both cases. Regardless of the length of the combustor, an analogous liner surface temperature curve was obtained under the same operating conditions and generalized initial test conditions (inlet pressure, inlet temperature, and mass flow). Since the distance between the two temperature measurement nodes of '$p3$' and '$p4$' is 250 mm, the exact interpretation on the flame length would not be feasible due to the insufficient data within

Table 6 Characteristic acoustic frequency (Hz) of the single liner configuration

Test temperature	Experimental	Analytical	FEM	FVM	Analytical†	FEM†	FVM†
${}^{(s)}T_{\text{room}}$	84	82 (2.4)	91 (8.3)	92 (9.5)	80 (4.8)	89 (6.0)	90 (7.1)
${}^{(s)}T_{60\text{-}1.6}$	163	165 (1.2)	175 (7.4)	171 (4.9)	161 (1.2)	170 (4.3)	166 (1.8)
Difference (%)	94	101	92	86	101	91	84

Note: the superscript symbol '†' denotes the end correction.

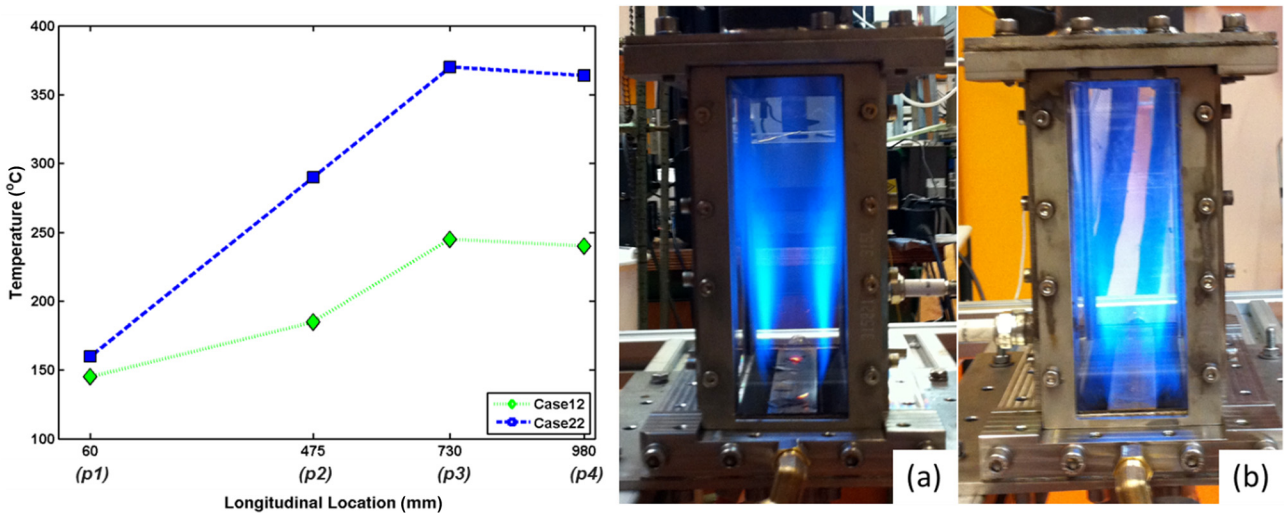

Fig. 15 Liner surface temperature profile and flame profile for (*a*) case 12, stable, and (*b*) case 22, unstable

these two nodes. However, the relative flame occupying the cross-section area of the stable and unstable combustion flame differs (see Fig. 15). The turbulence advances the flame speed in gaseous fuel-air mixtures and elevates the burning rates in gas turbine engines [53]. According to Damkohler [54] and Schelkin [55], the burning velocity is related to the turbulence intensity; hence, the wrinkled flame front that increases the specific flame surface area yielding an increase in the fresh mixture consuming ability. Hence, the temperature levels are proportionally increased. The aforementioned findings imply that the system instability is associated with elevated pressure levels and increased structure temperatures in comparison to the stable system (single liner) under the same initial operating conditions.

Note that the start-up of the experiments was held relative by progressing the input parameters up to the desired test case settings within the time-to-start to sustain the initial experimental conditions. The structure was gradually heated up, avoiding thermal shocks in the start-up periods, and it was air-cooled down in the shut-off periods.

3.7 Acoustic Characterization. The acoustic modal properties of the combustor test system with the single and double liner configurations at room temperature and at the operation temperature (cases 12 and 22) were experimentally, analytically, and numerically characterized. Note that hereafter, the single liner configuration will be denoted as the superscript '(s)' and the double liner is denoted as '(d)'. From the previous experiments [47], the acoustic boundary conditions of the combustor downstream were obtained by means of the reflection coefficient (R) that are closed ($R=1$) at one end ($x_c=0$, where the wedge is located) and open ($R=-1$) at the other end ($x_o=$ the height of the combustor downstream). The end conditions for the single ($x_o{}^s - x_c{}^s$) and double ($x_o{}^d - x_c{}^d$) liner configurations can be seen in Fig. 7. Furthermore, the mean temperature was measured as 1200 K inside the downstream part for the initial operating conditions of 60 kW power and a 1.6 air-fuel ratio. The acoustic eigenfrequencies of a rectangular volume (combustor) for the open-closed end condition are calculated by the following equation [26]:

$$f_{ijk} = \frac{c}{2}\sqrt{\left(\frac{i}{2L_x}\right)^2 + \left(\frac{j}{L_y}\right)^2 + \left(\frac{k}{L_z}\right)^2} \tag{12}$$

where c is the speed of sound, i, j, and k are the number of half waves in the three length directions (L_x, L_y, and L_z) associated with the x, y, and z coordinates (height, width, and depth of the combustor), respectively. For the first mode, the quarter-wave acoustic mode A (1,0,0), the equation is simplified as $f=c/4L_{\text{eff}}$, where L_{eff} is the effective length. The effective length of a closed-open end tube is given as $L_{eff}=L_x+(R_r)(a_{\text{tube}})$, where R_r is the radiation resistance that is taken as '0.6' and a_{tube} is the radius of the tube opening [56]. Note that the combustor in this work has a rectangular cross section. Therefore, this area is related to a tube opening cross section, which has the same area of the combustor in order to obtain an equivalent radius to calculate the effective length. The numerical results were calculated using an FEM code in the commercial software ANSYS and a finite volume method (FVM) Helmholtz solver AVSP. The reader is referred to the Ref. [47] for more information on the AVSP. The characteristic acoustic frequency of the combustor without mean flow is presented in Table 6 for the single liner configuration at room temperature (T_{room}) and at 1200 K ($T_{60\text{-}1.6}$) and in Table 7 for both the single and double liner configurations at $T_{60\text{-}1.6}$. These frequencies correspond to the first quarter-wave acoustic mode A [1,0,0] of the combustor. In the presented results, the superscript '†' denotes that the end correction is applied and the deviation in the results compared to the experimental results are specified in parentheses. As presented in the tables, the experimental results showthe deviation compared with the predicted results that is attributed to some parameters that are not included in the numerical model such as the possible acoustic damping presence in the combustor test setup and the additional volume created by the semi-infinite hoses attached to the combustor to avoid the high temperature effect in the piezoelectric pressure transducers. Furthermore, in the analytical calculation the entire geometry is assumed to have the same cross section; however, the depth of the upstream part of the combustor is half of the downstream part. However, the analytical results show a good coherence at both room and high temperatures for the single liner configuration. On the contrary, the acoustic response of the double liner configuration is accurately predicted by numerical calculations. The direct proportionality of the eigenfrequencies to the speed of sound, and considering that the speed of sound is proportional to the square root of the temperature, results in an apparent jump in the characteristic acoustic frequency of the single liner configuration at a mean temperature of $T_{60\text{-}1.6}$ inside the combustor. As seen in Table 7, a reduction in the range of 32–37% of the characteristic acoustic frequency is obtained when the liner is doubled, which is due to the larger acoustic period.

3.7.1 Structural Characterization. The structural modal characterization of the combustor test system was performed and the results were experimentally and numerically validated. Two experimental techniques were used: the roving hammer impact test

and the shaker test, as described in Sec. 3.4. The autospectra of the output signals were averaged over all of the measurement grid points. Hence, all the modes can be captured and missing a mode due to a measurement on the node point was avoided. The experimental and numerical results for the mode shapes and the eigenfrequencies of the first seven modes are presented in Fig. 16 and Table 8, respectively. Note that the measurements are performed on the liner only (see Fig. 7). The results show that the mode shapes are captured well. Furthermore, the predicted structural eigenfrequencies show good agreement with the measurements, except for two modes (first-torsional $t(1)$ and the second-bending $b(2)$ modes) in Table 8. In these modes, a large deviation was observed. This deviation is attributed to the production technique of the combustor test system. The downstream liner is composed of two L-shaped profiles welded together to form its rectangular geometry. The two opposite corners contain welds that can have an influence on the structural dynamic behavior [57]. The corner welds increase the local stiffness; thus, they increase the rigidity and act as a stiffener. Therewith, particularly, these torsional and bending modes appear to be shifted further within the mode sequence. This finding is attributed to the following reasons. As seen from the mode shapes in Fig. 16, the liner structure deforms with a limited amount of flexure in the first bending mode; thus this mode suffers less from the weld effects. However, in the second bending mode the corner welds experience a significant deflection and thus plays a role in the dynamic behavior. Furthermore, as seen from the experimental results in the second torsional mode, the deformation of the structure is restricted in the liner geometry, whereas the structure deforms together with the flame-box in the numerical results. Hence, the deviation between the

Table 8 Structural eigenfrequencies (Hz) of the single liner configuration at (T_{room})

Mode	Shaker testing	Impact testing	Average-testing	FEM
Bending, $b(1)$	125	125	125	126 (0.8)
Torsional, $t(1)$	534	534	534	437 (18.2)
Plate, $p(1)$	639	640	639.5	633 (1.0)
Bending, $b(2)$	645	645	645	532 (17.5)
Plate, $p(2)$	673	673	673	671 (0.3)
Plate, $-p(3)$	744	742	743	750 (0.9)
Torsional, $t(2)$	764	765	764.5	761 (0.5)

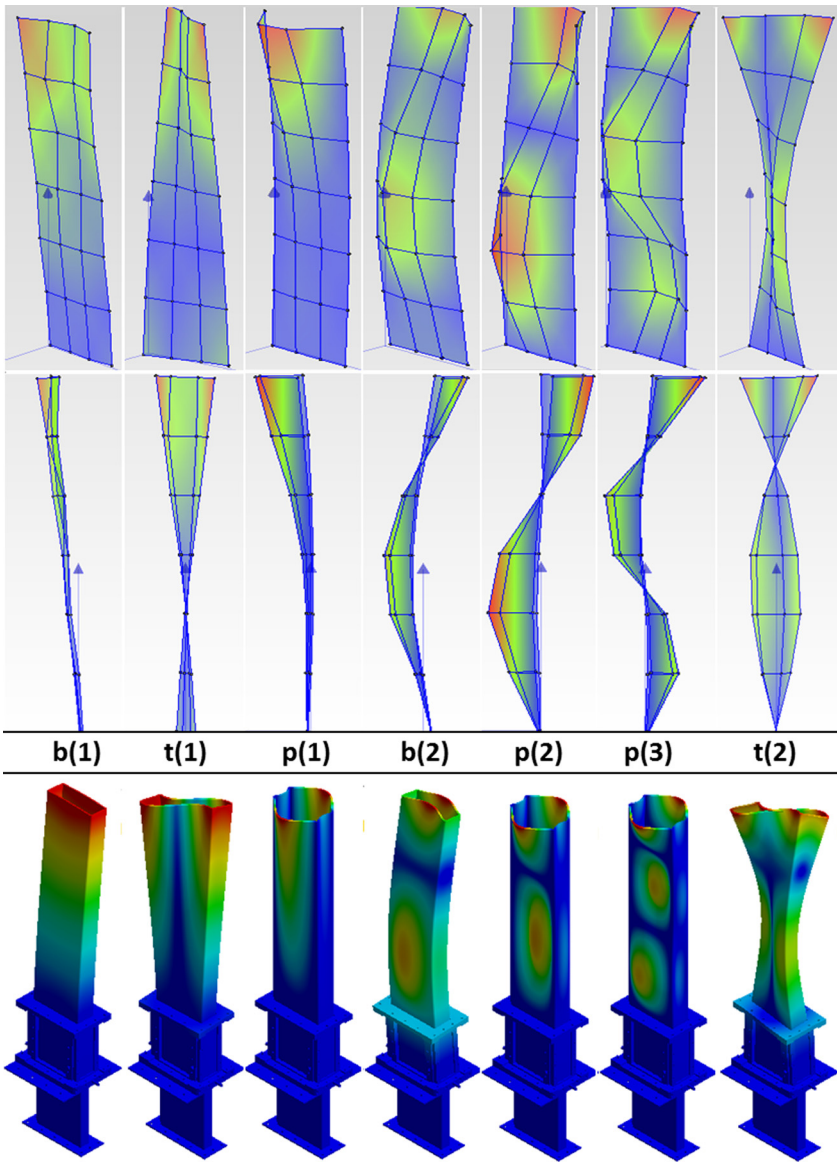

Fig. 16 Mode shapes of the single liner configuration (top: experiment; bottom: FEM)

measurement and simulation caused by the welding is hindered in this mode $t(2)$. The corner weldments require an approximate modeling to accommodate the overall modal analysis. However, the unknown material properties and the inhomogeneity of the weld turned down the numerical efforts for a better prediction of the eigenfrequencies. Considering that the plate modes of the structure are crucial for the acoustic response of the combustor due to the change in the acoustic volume (expansion and contraction of the volume) during the combustion process, the numerical results are claimed to be a good prediction, taking note of these remarks. For further analysis, the modal characterization of the double liner configuration was performed numerically.

It can be remarked that welds are the local discontinuous regions where fatigue cracks can occur. Residual stresses can be generated in weldments due to thermal expansion, plastic deformation, and shrinkage during cooling [58]. Even low-level residual stresses can significantly enhance the cracking behavior in structures [58,59] such as in combustion liners [60]. Besides, the welds can alter the structural dynamics due to the local stiff regions and dimensional inhomogeneity of the weld. Therefore, welding should be avoided in the design of the combustors under possible circumstances.

Since the combustion liner material is exposed to elevated temperatures during the combustion operation, the temperature dependence of the material properties must be considered. The surface temperature in the tests for case 22 was observed to vary between 160–370 °C (see Fig. 15). The eigenfrequencies of the specimen scale by the square root of Young's modulus. Hence, a temperature increase from room temperature to the maximum temperature of 370 °C ($T^w_{\text{case 22}}$) causes a reduction of about 15% of the Young's modulus of the liner material and, thus, the eigenfrequencies decrease by approximately 8%. The temperature dependency of the material properties is limited within this range (see Fig. 9), therefore, the maximum temperature was used as a homogeneous structural temperature in the numerical model. In Table 9, the FEM results are presented for single and double liner configurations at T_{room} and $T^w_{\text{case 22}}$. In the table, for the double liner configuration 'top' and 'bot' define the location of the mode, which is active either in the top or bottom liner, as depicted in Fig. 17 for the first two plate modes.

3.8 Acoustical and Structural Response. In this section, the acoustic and the structural responses of the combustor test system, with double liner configuration, during the combustion process are described. The acoustic, combustion, and structure domains are interlinked in the experimental results and the observed characteristics of the stable and unstable combustion are discussed. The temperature influence on the acoustic behavior at $T_{60\text{-}1.6}$ and structural behavior $T^w_{\text{case 22}}$ was investigated in the previous sections. The sound pressure level (SPL) and the liner wall velocity (υ) measurements in the time and frequency domain are depicted in Fig. 18 for the unstable combustion case 22. In the figure, the pressure signal at the three measurement locations, $p2$, $p5$, $p7$, and vibration signal at the $p3$ location are shown. The combustion instability generated a turbulent flame, high amplitude pressure oscillations, and a nonlinear system, including higher-order harmonics of the characteristic frequency but a deterministic vibration behavior with a well-shaped cyclic pressure and corresponding vibration of the liner.

Table 9 Predicted structural eigenfrequencies (Hz)

Mode number	Single T_{room}	Single $T^w_{\text{case 22}}$	Double T_{room}		Double $T^w_{\text{case 22}}$	
$p(1)$	663	610	(top) 628	(bot) 648	(top) 578	(bot) 596
$p(2)$	671	617	(top) 666	(bot) 714	(top) 613	(bot) 657
$p(3)$	750	690	(top) 743	(bot) 829	(top) 684	(bot) 763
$p(4)$	875	805	(top) 865	(bot) 995	(top) 796	(bot) 915

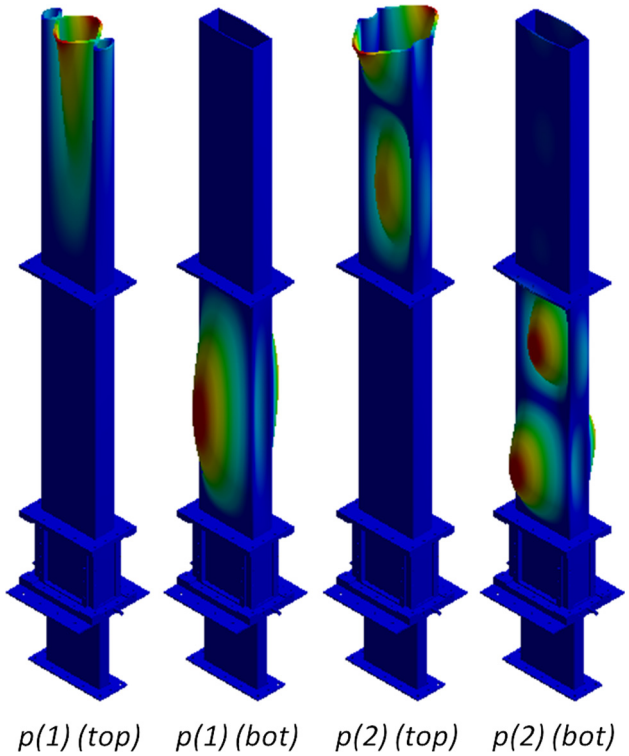

Fig. 17 First two plate modes in the double liner configurations

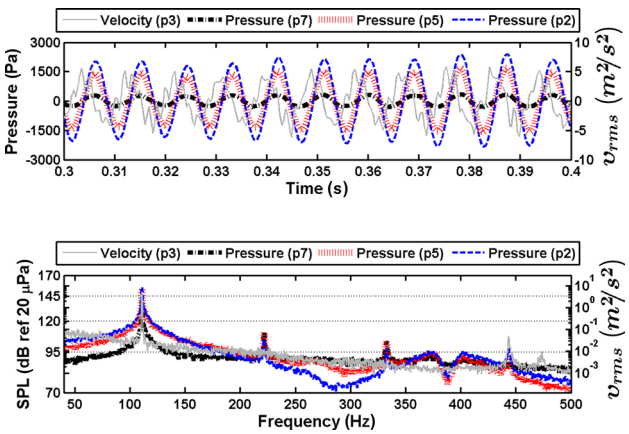

Fig. 18 Time signal and autospectrum of the acoustic pressure and velocity of the wall (case 22): (the measurement locations are shown in parentheses)

The SPL and vibration of the liner wall within the range up to 1000 Hz for cases 21 and 22 are shown in Figs. 19 and 20. The y-axis is rescaled in each plot to give a close-up view of the peaks. The higher-order harmonics of the limit cycle frequency are defined by the dashed lines in order to distinguish the modal frequencies from those harmonics. In case 22, seven more higher-harmonics of the characteristic frequency appeared in the 0–1000 Hz range. The generated pressure excites the combustor structure at these higher-harmonic frequencies. The reasons for the deviation in the observed eigenfrequencies in the experiments, compared to the numerical results, can be due to the use of a mean temperature value instead of the full temperature profile of the fluid and the structure. Besides, unstable combustion is a complex phenomenon and develops varying recirculation zones above the wedge of the combustor; therefore, the acoustic excitation is not completely uniform inside the combustor. The asymmetrical

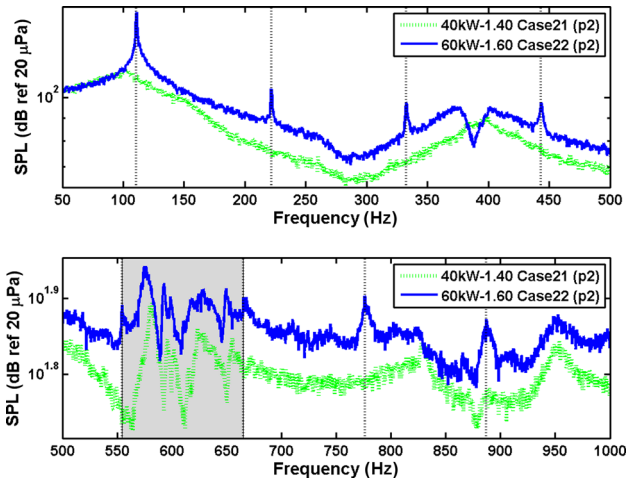

Fig. 19 SPL inside the combustor

structural dynamics caused by the corner welding and the fact that the measurement devices are mounted on one side of the combustor contribute to the overall deviation. In the numerical analysis, the effect of the surrounding fluid in the structural dynamics was neglected; however, the structural dynamics adjacent to a fluid domain generally couples to the fluid motion. Thus, the fluid affects the structure as damping forces and an added mass. The damping of the plate will be increased, accounting for the fluid and its state. The added mass represents the fluid inertia related to the acceleration of the structure and, consequently, the back-relation of the surrounding fluid acceleration. Hence, the effective mass and the effective mass moment of inertia of the structure are increased by the added mass components of the fluid inside the combustor with two-way interaction. The following equation [26] can approximately describe the effect of the added mass on the eigenfrequencies, due to the fact that the eigenfrequency of an elastic structure is inversely proportional to the square root of the mass

$$\frac{f_i^{\text{fluid medium}}}{f_i^{\text{vacuum medium}}} = \frac{1}{\left(1+\frac{A_p}{M_p}\right)^{1/2}} \tag{13}$$

where M_p is the mass of the structure and A_p is the added mass that is generally a function of the structure geometry, boundary conditions and mode number, fluid properties, and the fluid state. In this equation, the mode shapes are assumed to be preserved and the effect of the air surrounding the combustor from outside is assumed to be negligible. Thus, it can be concluded that the acousto-elastic coupling, which was described in Sec. 2, is expected to contribute to the changes in eigenfrequencies observed in the experiments.

The shaded areas in Figs. 19 and 20 represent the frequency range of the 4th and 5th harmonics of the characteristic frequency. In this range, the structural eigenfrequencies belonging to the first and the second plate modes take place. The expansion and contraction motion of the walls, due these modes, alters the acoustic volume of the combustor and, thus, the pressure inside. Hence, the structure to fluid interaction is stimulated and the acoustic pressure is coupled to the wall vibrations. The shaded areas are depicted in Fig. 21. In the figure, the velocity peaks are marked and the corresponding frequencies (vertical dashed lines) are matched in the pressure spectrum. The frequencies of the peaks in both plots are in agreement. However, the wall vibration peaks enclosed with the rectangular dotted-frame in the figure are found to have limited influence on the pressure. The measured frequencies, where the significant peaks are located, and the FEM results are listed in Table 10. The results are in good agreement, except for the frequency of 599 Hz. In this frequency, the pressure amplitudes reach a local-peak at the '$p2$' and '$p5$' locations; however, this behavior is not responsive at the '$p7$' location. Thus, even though the plate modes of the structure interact with the fluid, the main driving mechanism of the thermo-acoustic instability remains independent from these modes, since the characteristic frequency is much lower than the eigenfrequencies belonging to these modes. At the characteristic frequency, a strong fluid-to-structure interaction is generated due to the combustion-driven instability. This results in the highest amplitude of the wall vibrations of the structure at the characteristic frequency.

3.9 Structural Damage Monitoring. The presence of damage in the structure leads to a change in the modal parameters. Since the responsiveness of the modal parameters depends on the severity and the location of the damage, the changes in the modal parameters are not identical. Therefore, dynamic testing was conducted during the combustion operation by means of the frequency shift technique and the flexibility method. The vibration of the plate specimen attached to the flame-box was continuously monitored at the half-diagonal node points to ensure that all modes are covered in the assessment. In the figure, '$\upsilon_{\text{node no.}}$' is used to identify the velocity of the measured node number on the scan grid (Fig. 22).

Two experiments were carried out: one on the intact and one on the damaged specimen attached to the flame-box and the

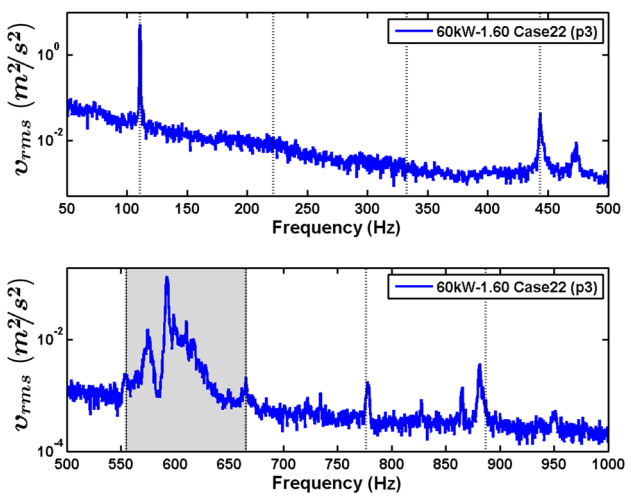

Fig. 20 Velocity amplitude of the liner wall

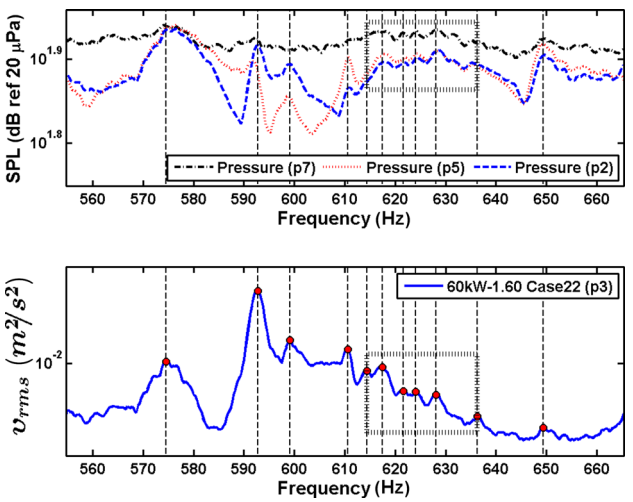

Fig. 21 SPL and the velocity amplitude of the liner wall

Table 10 Experimental and numerical comparison of the frequencies (Hz)

Experiment	FEM	Mode	Deviation (%)
575	578	$p(1)$ (top)	0.5
593	596	$p(1)$ (bot)	0.5
599	—	—	—
611	612	$p(2)$ (top)	0.2
649	657	$p(2)$ (bot)	1.2

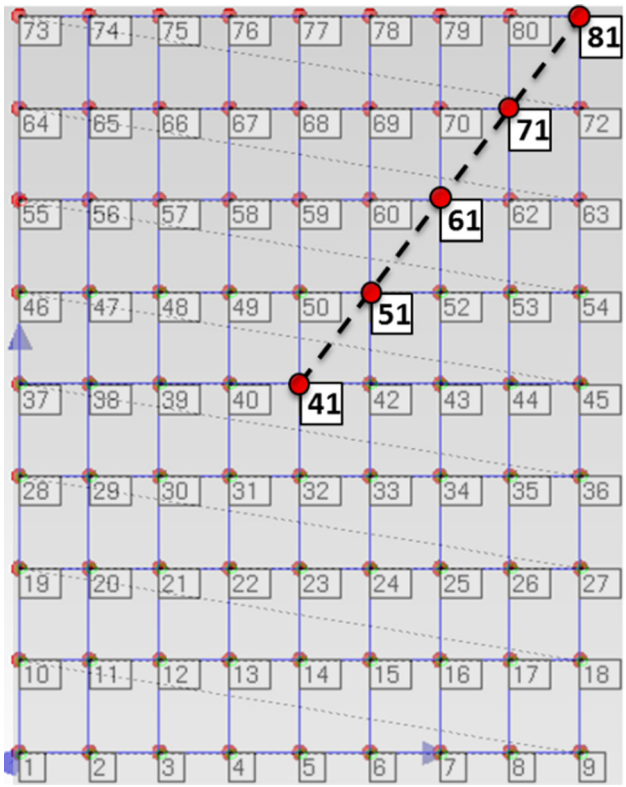

Fig. 22 Measurement grid (9 × 9: $\upsilon_{\text{node no.}}$)

combustor was set to case 22, where the combustion instabilities were observed. Since the abnormal loss of the stiffness due to damage will be reflected as a reduction of the measured eigenfrequencies, the damage detection algorithm infers the existence of the damage by the eigenfrequency shift. The stochastic nature of the instability exhibits identical characteristic frequencies but different pressure amplitudes at the higher-harmonics of the characteristic frequencies. Thus, the specimen was excited with different pressure levels that lead to different vibrations. Therefore, the velocity amplitudes at each node are normalized with respect to its maximum amplitudes and pressure to avoid differing pressure levels (see Figs. 23 and 24). Note that the superscript '∼' denotes normalization. In Fig. 23, the pressure (at the '$p7$' location) and velocity measurements are depicted, belonging to the intact and the damaged cases for the 0–1000 Hz range. The ranges of the y-axes in the figures are identically set. In the damaged specimen, 'node 41' coincides with the damage location; thus, the corresponding velocity data is not available.

Since the unstable combustion generated distinct acoustic pressures at four frequencies until 444 Hz, the vibration behavior was dominated by these pressures in this range. Therefore, the investigation frequency range was scaled down to 445–610 Hz in order to distinguish the structural eigenfrequencies of the system from the frequencies of the dominant acoustic pressures. In Fig. 24, the vertical lines represent the higher-harmonic frequencies of the characteristic (limit-cycle oscillation) frequency (solid line), the peak frequency marking for the intact specimen (dotted line), and for the damaged specimen (dashed-dotted line). Inside each pocket (between two adjacent higher-harmonic frequencies), one distinct peak frequency pair was marked in both the intact and damaged plots. The average reduction of representative frequencies in the presented frequency range is less than 1.5%. The frequency shift method was, therefore, found to be insensitive to the current damage configuration.

Next, the local response of the structure was investigated under the instability pressure peaks. A new method is proposed, the so-called instability peaks method, which is based on the change of dynamics behavior of the structure at characteristic and higher-harmonic frequencies. In Fig. 25, the normalized velocity measurement at each distinct frequency (characteristic frequency and harmonics), which is normalized here by the characteristic frequency ($\hat{f}$), is presented, including both intact and damaged cases. As previously discussed, $\upsilon_{\text{node 41}}$ for the damage case is not available; hence, its maximum normalized amplitude does not reach one at any of the distinct frequencies. Furthermore, the maximum amplitude of $\upsilon_{\text{node 81}}$ is at the second frequency (first harmonic of the characteristic frequency) in the intact case, whereas in the damaged case its location shifts to the first frequency, which can be attributed to the local mode change due to the damage. Furthermore, in Table 11 the absolute deviation of $\hat{\upsilon}_{\text{rms}}$ of the damaged configuration from the intact configuration and the average of each row (Average υ, velocity component based) and column (Average f, frequency component based) are presented. Here, $\upsilon_{\text{node 41}}$ is excluded from the table due to the aforementioned reasons. As seen from the table, the highest difference between the intact and

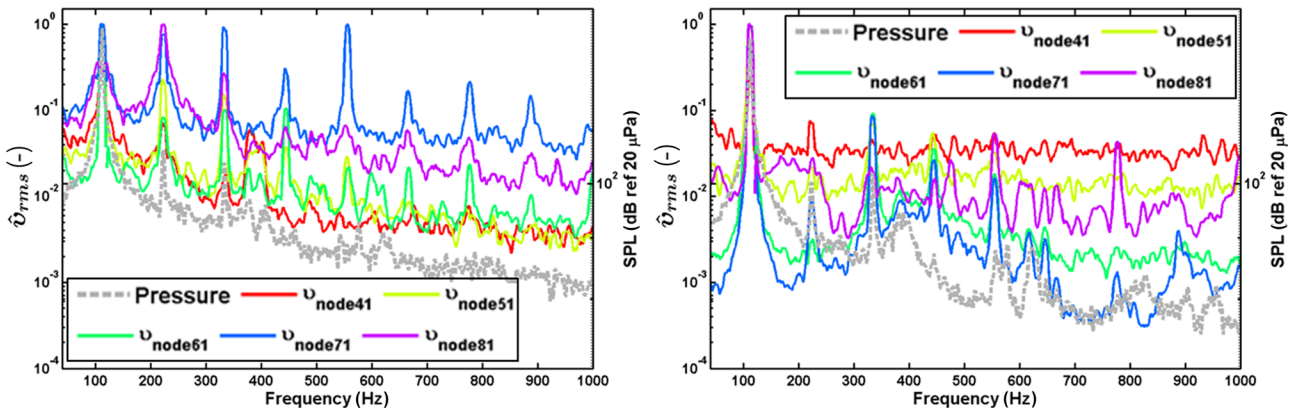

Fig. 23 Cross-correlations of the pressure (at $p7$) and the velocity of the diagonal-nodes ($\upsilon_{\text{node\#}}$) of the intact (left) and damaged (right) specimen

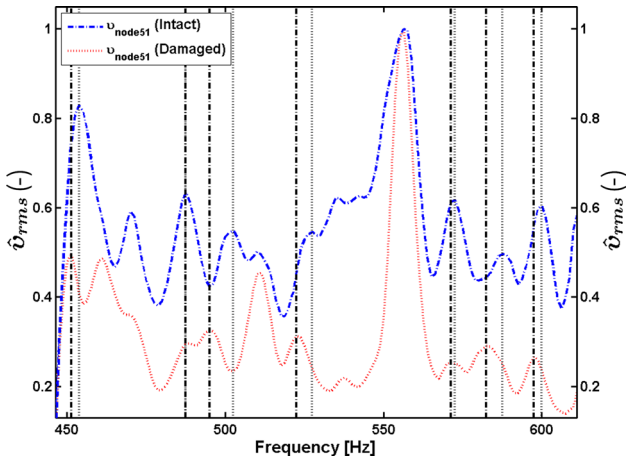

Fig. 24 Laser zigzag path generation and nodal surface scanning grid and structural vibrations comparison

damaged configurations is at the 'node 51' location and the ninth frequency (eight harmonic frequency). This node is the closest measurement location to the damage that leads to the highest change in the velocity amplitude. Furthermore, the sensitivity of the ninth frequency is attributed to local mode alteration due to the damaged state. However, this method is not reliable to predict the damage location, since the combustion process generates complex behavior that can lead to a misinterpretation. Moreover, the method requires a prior numerical analysis in order to obtain the structural modes and define the contribution of the frequency content from the graph.

The frequency shift and instability peaks response methods are not found to be robustly predictive in structural damage monitoring. Therefore, the vibration measurement is performed on a 9×9 scan grid in the whole specimen area and the flexibility method is applied using two sets of data (intact and damaged cases). The results are depicted in Fig. 26. The highest flexibility was found on the sides of the center-crack type of damage. The flexibility method captured the damage existence, location, and severity.

The influence of damage in the structural dynamics was covered up to this point by means of the modal parameters and the flexibility. The damage can progress during the operation, not only by cyclic pressure amplitudes but also due to the elevated

Table 11 Deviation (%) of $\hat{\upsilon}_{\text{rms}}$ with respect to the intact and damaged configurations

$\hat{f}$	1	2	3	4	5	6	7	8	9	Average υ
$\upsilon_{\text{node 51}}$	0.0	90.6	54.7	48.0	13.2	76.0	207.4	214.9	361.5	118.5
$\upsilon_{\text{node 61}}$	0.0	98.0	9.4	66.3	16.4	90.4	89.2	75.5	90.0	59.5
$\upsilon_{\text{node 71}}$	0.0	98.9	90.8	91.5	98.4	99.3	99.4	97.3	97.3	85.9
$\upsilon_{\text{node 81}}$	283.0	98.1	93.4	87.9	20.2	77.5	10.5	69.6	55.6	88.4
Average f	70.7	96.4	62.1	73.4	37.1	85.8	101.6	114.3	151.1	

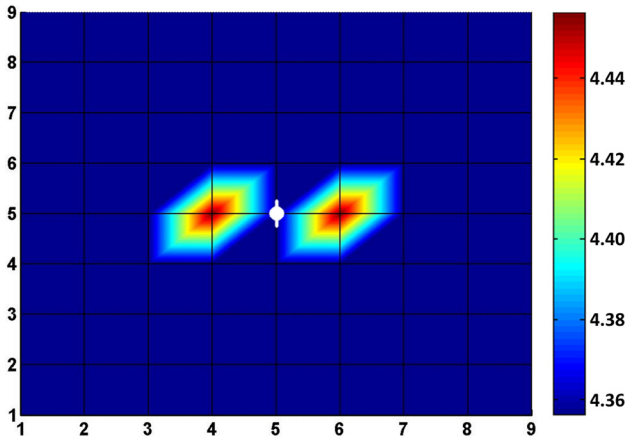

Fig. 26 Damage localization due to the change in the flexibility matrix

temperature exposure. Furthermore, the thermal gradient presence can enhance the deterioration of the component. The IR camera method was used to obtain the temperature profile evolution on the specimen during the operation. The comparative test results for both the intact and damaged specimens are shown in Fig. 27. The color bar is depicted as a representative spectrum in order to emphasize the distinct temperature field in each frame. In the intact specimen case the temperature increase starts locally and spreads to the upper body as the hot combustion gas flows, whereas in the damaged case the temperature increase concentrates around the introduced damage. This can lead to a reduction

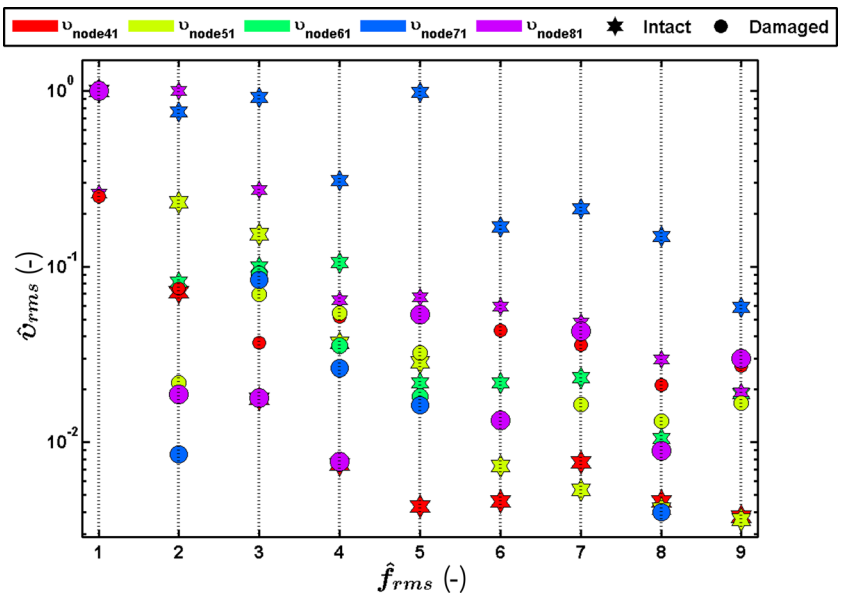

Fig. 25 Structural response to instability peaks

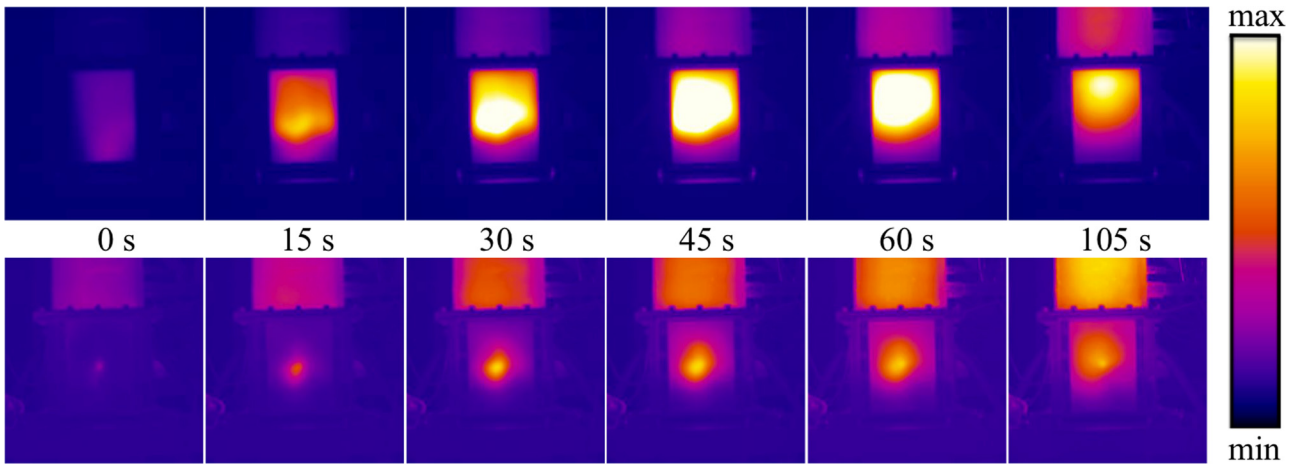

Fig. 27 Temperature evolution on the intact (above) and damaged (below) specimens

of the material strength due to the temperature-dependent properties. The hot gases leaked out through the damage, potentially causing an additional temperature gradient across the structure interacting with the atmospheric environment under this condition. In general, the plastic work fields around the crack tip generate thermal energy due to plasticity and, hence, temperature fields, which leads to a softening of the material [61]. The sustained intense thermal stresses at the damage location can elevate the energy release rate along the crack front and, thus, the crack driving forces [62]. Therefore, the intensified temperature rise at the damage location would lead to an accelerated crack growth compared to the initial design conditions.

4 Concluding Remarks and Discussion

The conclusions of this multiphysical investigation covering combustion, acoustics, and vibration phenomena, can be drawn mainly as follows:

- Limit-cycle pressure oscillations due to combustion instabilities can be generated in the generic combustor test system on demand. The operating points, which induce instabilities, are defined in the instability map.
- The higher-order harmonics of the combustion characteristic frequency due to the nonlinear nature of the combustion instability was generated. Since the harmonics spread over a large frequency band with respect to the order-number, a possible concurrence/interaction of those harmonics with the structural modes of the system is unavoidable. Yet, the full explanation for the number of fairly high amplitudes of the harmonics and the occurrence of the feedback mechanisms that damp some acoustic oscillations is deficient. This effect becomes crucial in designing instability control systems (and its frequency range) for gas turbine engines.
- The generic combustor test system in this work is a basic prototype of an industrial system, which enables an easy operation and validation of numerical calculations with well-defined boundary conditions in a cost-effective manner. Consequently, the test system enables a robust investigation of the combustion-acoustics-structure interrelation under limit cycle conditions. Besides, several variances and analogies between the test system and industrial combustion systems were described throughout the paper. Nevertheless, the methodology for the structural dynamics assessment was proven to be valid and feasible up to a reasonable complexity. Therefore, the core of the modeling procedure can be used to achieve the desired accuracy and complexity by including the circumstances belonging to industrial combustors.
- A real-time combined vibration and thermal based structural assessment method, consisting of an LDV, an infrared camera, and a programmable traverse system, was integrated in the combustor test system and enables working continuously during the experiments. The progressive variation in the structural response and the temperature profile were monitored and characterized under combustion driven dynamic loading conditions. The generated pressure was coupled with the structure vibrations in the limit cycle condition. Structural damage detection, localization, and severity quantification was successfully performed by using a combined flexibility and thermography method. For the flexibility method, only a few of the lower modes are sufficient for the measurement to obtain an accurate calculation of the change in the flexibility matrix. The thermography method enables measurement of the full-field in image form and a fast evaluation. In addition, the thermography method showed that the temperature was localized around the damage, which is in contrast to the intact case during the combustion operation. This leads to an accelerated damaging process due to localized softening of the material.
- It should be noted that the variation of the thermal expansion coefficient due to the temperature change can cause a prestress effect. The specimen holder in the generic combustion test system enables the specimen to slide inside the fixture due to expansion in the longitudinal and transverse directions. This mechanism partially compensates for the thermal expansion; however, the prestress can still remain due to the friction.

Acknowledgment

The authors would like to acknowledge funding of this research by the EC in the Marie Curie Actions–Networks for Initial Training, under Call No. FP7-PEOPLE-2007-1-1-ITN, Project LIMOUSINE with Project No. 214905. Additionally, the authors would like to thank J. C. Roman Casado and M. Kapucu from the University of Twente Thermal Engineering Department for the experimentation assistance.

Nomenclature

a_c = crack length
a_o = initial crack length
A_p = added mass
a_{tube} = radius of the tube opening
$A(i,j,k)$ = acoustic mode representation
B = thickness
c = speed of sound
$\mathbf{C}$ = coupling matrix

d_c = crack diameter
E = Young's modulus
f = frequency
$\mathbf{F}^f$ = fluid load vector
$\mathbf{F}^s$ = structural load vector
$\mathbf{G}$ = flexibility matrix
$\mathbf{G}_\Delta$ = flexibility-change matrix
$\mathbf{K}$ = stiffness matrix
$\mathbf{K}^f$ = assembled fluid equivalent "stiffness" matrix
$\mathbf{K}^{fs}$ = assembled coupling "stiffness" matrix
$\mathbf{K}^s$ = assembled structural stiffness matrix
L = length
$\mathbf{M}$ = mass matrix
M_p = mass of the structure
$\mathbf{M}^f$ = assembled fluid equivalent "mass" matrix
$\mathbf{M}^{fs}$ = assembled fluid-structure coupling "mass" matrix
$\mathbf{M}^s$ = assembled structural mass matrix
$\mathbf{P}$ = nodal pressure vector
p' = pressure oscillation
p_{1-7} = measurement locations
q' = heat release perturbation
R = reflection coefficient
R_r = radiation resistance
S_{1-4} = test combustor part numbers
$S(i,j)$ = structural mode representation
t = time
T = temperature
$\mathbf{u}$ = nodal displacement vector
V = volume of the domain
W = width
w_c = crack width
x = length coordinate
γ = mass per unit area of the plate
δ_{lm} = elements of $(\mathbf{G}_\Delta)$
λ_{ij} = dimensionless frequency parameter
ρ = density
τ = period of the oscillation
υ = Poisson's ratio
υ = liner wall velocity
ϕ = wave energy dissipation
$\mathbf{\Phi}$ = mode shape matrix
ω = modal frequency
$\mathbf{\Omega}$ = modal stiffness matrix

Subscripts

d = damaged
eff = effective
h = intact
i, j, k = mode shape number indicators
m = index for the damaged element
n = number of degrees of freedom
node number = measurement node number
p = plate
x, y, z = Cartesian coordinate indicators

Superscripts

d = double liner configuration
s = single liner configuration
w = liner wall
† = end correction
$\sim$ = normalization

Abbreviations

AE = acoustic emission
DAQ = data acquisition system
DOF = degree of freedom
FEM = finite element method
FVM = finite volume method
IR = infrared
LDV = laser Doppler vibrometer
SPL = sound pressure level
VB = vibration-based

References

[1] Lieuwen, T., Torres, H., Johnson, C., and Zinn, B. T., 2001, "A Mechanism of Combustion Instability in Lean Premixed Gas Turbine Combustors," ASME J. Eng. Gas Turbines Power, **123**(1), pp. 182–189.
[2] Rayleigh, J. W. S., and Lindsay, R. B., 1945, *The Theory of Sound*, Dover, New York.
[3] Crocker, D. S., Nickolaus, D., and Smith, C. E., 1999, "CFD Modeling of a Gas Turbine Combustor From Compressor Exit to Turbine Inlet," ASME J. Eng. Gas Turbines Power, **121**(1), pp. 89–95.
[4] Rao, M. S., and Sivaramakrishna, G., 2009, "Performance Improvement of an Aero Gas Turbine Combustor," ASME Paper No. GT2009-59928.
[5] Kim, W.-W., Van Slooten, P. R., Malecki, R. E., Syed, S., Colket, M. B., and Lienau, J. J., 2006, "Towards Modeling Lean Blow Out in Gas Turbine Flameholder Applications," ASME J. Eng. Gas Turbines Power, **128**(1), pp. 40–48.
[6] McGuirk, J. J., and Spencer, A., 2001, "Coupled and Uncoupled CFD Prediction of the Characteristics of Jets From Combustor Air Admission Ports," ASME J. Eng. Gas Turbines Power, **123**(2), pp. 327–332.
[7] Bain, D. B., Smith, C. E., Liscinsky, D. S., and Holdeman, J. D., 1999, "Flow Coupling Effects in Jet-in-Crossflow Flowfields," J. Propul. Power, **15**(1), pp. 10–16.
[8] Tinga, T., van Kampen, J. F., de Jager, B., and Kok, J. B. W., 2007, "Gas Turbine Combustor Liner Life Assessment Using a Combined Fluid/Structural Approach," ASME J. Eng. Gas Turbines Power, **129**(1), pp. 69–79.
[9] Bradley, D., Gaskell, P. H., Gu, X. J., Lawes, M., and Scott, M. J., 1998, "Premixed Turbulent Flame Instability and NO Formation in a Lean-Burn Swirl Burner," Combust. Flame, **115**(4), pp. 515–538.
[10] Cohen, J. C., and Anderson, T., 1996, "Experimental Investigation of Near-Blowout Instabilities in a Lean, Premixed Step Combustion," AIAA 34th Aerospace Sciences Meeting and Exhibit, Reno, NV, January 15–18, AIAA Paper No. 96-0819.
[11] Dowling, A. P., and Stow, S. R., 2003, "Acoustic Analysis of Gas Turbine Combustors," J. Propul. Power, **5**(19), pp. 751–763.
[12] Krebs, W., Flohr, P., Prade, B., and Hoffmann, S., 2002, "Thermoacoustic Stability Chart for High Intense Gas Turbine Combustion Systems," Combustion Sci. Technol., **174**, pp. 99–128.
[13] Hubbard, S., and Dowling, A. P., 2001, "Acoustic Resonances of an Industrial Gas Turbine Combustion System," ASME J. Eng. Gas Turbines Power, **123**(4), pp. 766–773.
[14] McManus, K. R., Poinsot, T., and Candel, S. M., 1993, "A Review of Active Control of Combustion Instabilities," Prog. Energy Combust. Sci., **19**(1), pp. 1–29.
[15] Lieuwen, T., 2003, "Modeling Premixed Combustion-Acoustic Wave Interactions: A Review," J. Propul. Power, **19**(5), pp. 765–781.
[16] Tufano, S., Stopford, P., Roman Casado, J. C., and Kok, J. B. W., 2012, "Modelling Flame-Generated Noise in a Partially Premixed, Bluff Body Stabilized Model Combustor," ASME Paper No. GT2012-69501.
[17] Junger, M. C., and Feit, D., 1972, *Sound, Structures, and Their Interaction*, MIT, Cambridge, MA.
[18] Fahy, F., and Gardonio, P., *Sound and Structural Vibration—Radiation, Transmission and Response*, 2nd ed., Elsevier, New York.
[19] Huls, R. A., van Kampen, J. F., van der Hoogt, P. J. M., Kok, J. B. W., and de Boer, A., 2008, "Acoustoelastic Interaction in Combustion Chambers: Modeling and Experiments," ASME J. Eng. Gas Turbines Power, **130**(5), p. 051505.
[20] Huls, R. A., Sengissen, A. X., van der Hoogt, P. J. M., Kok, J. B. W., Poinsot, T., and de Boer, A., 2007, "Vibration Prediction in Combustion Chambers by Coupling Finite Elements and Large Eddy Simulations," J Sound Vib, **304**(1–2), pp. 224–229.
[21] Khatir, Z., Pozarlik, A. K., Cooper, R. K., Watterson, J. W., and Kok, J. B. W., 2008, "Numerical Study of Coupled Fluid-Structure Interaction for Combustion System," Int. J. Numer. Methods Fluis, **56**(8), pp. 1343–1349.
[22] Alemela, R., Roman Casado, J. C., Kumar, S., and Kok, J., 2011, "Simulation of Limit Cycle Pressure Oscillation With Coupled Fluid-Structure Interactions in a Model Combustor," 18th International Congress on Sound and Vibration (ICSV 18), Rio de Janeiro, Brazil, July 10–14.
[23] Shahi, M., Kok, J. B. W., and Alemela, P. R., 2012, "Simulation of 2-Way Fluid Structure Interaction in a 3D Model Combustor," ASME Paper No. GT2012-69681.
[24] Altunlu, A. C., Shahi, M., Pozarlik, A., van der Hoogt, P. J. M., Kok, J. B. W., and de Boer, A., 2012, "Fluid-Structure Interaction on the Combustion Instability," 19th International Congress on Sound and Vibration (ICSV 2012), Vilnius, Lithuania, July 8–12.
[25] Visser, R., 2004, "A Boundary Element Approach to Acoustic Radiation and Source Identification," Ph.D. thesis, University of Twente, Enschede, Netherlands.
[26] Blevins, R. D., 2001, *Formulas for Natural Frequency and Mode Shape*, Robert E. Krieger, Malabar, FL.
[27] Cook, R. D., Malkus, D. S., and Plesha, M. E., 2002, *Concepts and Applications of Finite Element Analysis*, Wiley, New York.
[28] ANSYS® Academic Research, "Help System: Acoustics," Release 14.0, Ansys, Inc.
[29] Cawley, P., and Adams, R. D., 1979, "The Location of Defects in Structures From Measurements of Natural Frequencies," J. Strain Anal. Eng. Des., **14**(2), pp. 49–57.

[30] Stubbs, N., and Osegueda, R., 1990, "Global Non-Destructive Damage Evaluation in Solids," Int. J. Anal. Exp. Modal Anal., **5**, pp. 67–79.
[31] Salawu, O. S., 1997, "Detection of Structural Damage Through Changes in Frequency: A Review," Eng. Struct., **19**(9), pp. 718–723.
[32] West, W. M., 1986, "Illustration of the Use of Modal Assurance Criterion to Detect Structural Changes in an Orbiter Test Specimen," 4th International Modal Analysis Conference, Los Angeles, CA, February 3–6, pp. 1–6.
[33] Mayes, R. L., 1992, "Error Localization Using Mode Shapes—An Application to a Two Link Robot Arm," 10th International Modal Analysis Conference, San Diego, CA, February 3–6, pp. 886–891.
[34] Stubbs, N., Kim, J. T., and Farrar, C. R., 1995, "Field Verification of a Nondestructive Damage Localization and Severity Estimation Algorithm," 13th International Modal Analysis Conference, Nashville, TN, February 13–16, pp. 210–218.
[35] Ooijevaar, T. H., Loendersloot, R., Warnet, L. L., de Boer, A., and Akkerman, R., 2010, "Vibration Based Structural Health Monitoring of a Composite T-Beam," Composite Struct., **92**(9), pp. 2007–2015.
[36] Toksoy, T., and Aktan, A. E., 1994, "Bridge-Condition Assessment by Modal Flexibility," Exp. Mech., **34**(3), pp. 271–278.
[37] Pandey, A. K., and Biswas, M., 1994, "Damage Detection in Structures Using Changes in Flexibility," J. Sound Vib., **169**(1), pp. 3–17.
[38] Pandey, A. K., and Biswas, M., 1995, "Damage Diagnosis of Truss Structures by Estimation of Flexibility Change," Modal Anal., **10**(2), pp. 104–117.
[39] Doebling, S. W., Farrar, C. R., Prime, M. B., and Shevitz, D. W., 1996, "Damage Identification and Health Monitoring of Structural and Mechanical Systems From Changes in Their Vibration Characteristics: A Literature Review," Los Alamos National Laboratory, Los Alamos, NM, Report No. LA-13070-MS.
[40] Aktan, A. E., Lee, K. L., Chuntavan, C., and Aksel, T., 1994, "Modal Testing for Structural Identification and Condition Assessment of Constructed Facilities," 12th International Modal Analysis Conference, Honolulu, HI, January 31–February 3, pp. 462–468.
[41] Doebling, S. W., Farrar, C. R., and Goodman, R. S., 1997, "Effects of Measurement Statistics on the Detection of Damage in the Alamosa Canyon Bridge," 15th International Modal Analysis Conference, Orlando, FL, February 3–6, pp. 919–929.
[42] Farrar, C. R., Doebling, S. W., Cornwell, P. J., and Straser, E. G., 1997, "Variability of Modal Parameters Measured on the Alamosa Canyon Bridge," 15th International Modal Analysis Conference, Orlando, FL, February 3–6, pp. 257–263.
[43] Altunlu, A. C., van der Hoogt, P., and de Boer, A., 2011, "Life Assessment by Fracture Mechanics Analysis and Damage Monitoring Technique on Combustion Liners," ASME Paper No. GT2011-46107.
[44] Berman, A., and Flannell, W. G., 1971, "Theory of Incomplete Models of Dynamic Structures," AIAA J., **9**(8), pp. 1481–1487.
[45] Adams, R. D., Cawley, P., Pye, C. J., and Stone, B. J., 1978, "A Vibration Technique for Non-Destructively Assessing the Integrity of Structures," J. Mech. Eng. Sci., **20**(2), pp. 93–100.
[46] Huls, R. A., 2006, "Acousto-Elastic Interaction in Combustion Chambers," Ph.D. thesis, University of Twente, Enschede, Netherlands.
[47] Roman Casado, J. C., Alemela, P. R., and Kok, J. B. W., 2011, "Experimental and Numerical Study of the Effect of Acoustic Time Delays on Combustion Stability," 18th International Congress on Sound and Vibration (ICSV 18), Rio de Janeiro, Brazil, July 10–14.
[48] Haynes International, 2003, "High-Temperature Tech Brief: HAYNES® 230® Alloy," http://www.haynesintl.com/pdf/h3060.pdf
[49] Haynes International, "HAYNES® HR-120TM Alloy," http://www.haynesintl.com/pdf/h3125.pdf
[50] Roman Casado, J. C., and Kok, J. B. W., 2012, "Non-Linear Effects in a Lean Partially Premixed Combustor During Limit Cycle Operation," ASME Paper No. GT2012-69164.
[51] Lieuwen, T., and Neumeier, Y., 2002, "Nonlinear Pressure-Heat Release Transfer Function Measurements in a Premixed Combustor," Proc. Combust. Inst., **29**(1), pp. 99–105.
[52] Seo, S., 2003, "Combustion Instability Mechanism of a Lean Premixed Gas Turbine Combustor," KSME Int. J., **17**(6), pp. 906–913.
[53] Lefebvre, A. H., and Ballal, D. R., 2010, *Gas Turbine Combustion: Alternative Fuels and Emissions*, Taylor & Francis, Boca Raton, FL.
[54] Damkohler, G., 1939, "The Effect of Turbulence on the Flame Velocity in Gas Mixtures," Z. Elektrochem., **46**(11), pp. 601–626 (English translation: NACA Tech. Mem. No. 1112, 1947).
[55] Schelkin, K. I., 1943, "On Combustion in a Turbulent Flow," J. Tech. Physics (USSR) Vol. XIII(9–10), pp. 520–530 (English translation: NACA Tech. Mem. No. 1110, 1947).
[56] Blackstock, D. T., 2000, *Fundamentals of Physical Acoustics*, Wiley, New York.
[57] Palmonella, M., Friswell, M. I., Mottershead, J. E., and Lees, A. W., 2005, "Finite Element Models of Spot Welds in Structural Dynamics: Review and Updating," Comput. Struct., **83**(8–9), pp. 648–661.
[58] Link, L. R., 1990, "Fatigue Crack Growth of Weldments," Fatigue and Fracture Testing of Weldments (ASTM STP 1058), Sparks, NV, April 25, 1988, American Society for Testing and Materials, Philadelphia, PA, pp. 16–33, ASTM Paper No. STP24088S.
[59] Bucci, R. J., 1981, "Effect of Residual Stress on Fatigue Crack Growth Rate Measurements," 13th National Symposium on Fracture Mechanics (ASTM STP 743), Philadelphia, PA, June 16–18, American Society for Testing and Materials, Philadelphia, PA, pp. 28–47, ASTM Paper No. STP28789S.
[60] Kim, K. M., Yun, N., Jeon, Y. H., Lee, D. H., and Cho, H. H., 2010, "Failure Analysis in After Shell Section of Gas Turbine Combustion Liner Under Base-Load Operation," Eng. Failure Anal., **17**(4), pp. 848–856.
[61] Bhalla, K. S., Zehnder, A. T., and Han, X., 2003, "Thermomechanics of Slow Stable Crack Growth: Closing the Loop Between Experiments and Computational Modeling," Eng. Fract. Mech., **70**(17), pp. 2439–2458.
[62] Shih, C. F., Moran, B., and Nakamura, T., 1986, "Energy Release Rate Along a Three-Dimensional Crack Front in a Thermally Stressed Body," Int. J. Fract., **30**(2), pp. 79–102.